Manuscript cover page

Surface and Coatings Technology

Interface reactions of magnetron sputtered Si-based dual layer coating systems as oxidation protection for Mo-Si-Ti alloys

Ronja Anton [a,*], Steffen Hüning [b, a], Nadine Laska [a], Matthias Weber [c], Steven Schellert [c], Bronislava Gorr [d], Hans-Jürgen Christ [c], Martin Heilmaier [e], Uwe Schulz [a],

[a] German Aerospace Center (DLR), Institute of Materials Research, Cologne 51147, Germany

[b] Technical University (TU) Dortmund, now LIMO GmbH, Dortmund 44319, Germany

[c] University of Siegen, Institute for Materials Engineering, Siegen 57076, Germany

[d] Karlsruhe Institute of Technology (KIT), Institute for Applied Materials - Applied Materials Physics, Karlsruhe 76334, Germany

[e] Karlsruhe Institute of Technology (KIT), Institute for Applied Materials – Materials Science and Engineering, Karlsruhe 76334, Germany

*Corresponding author. E-mail: ronja.anton@dlr.de, Tel: +49 2203 601 2134, Fax: +49 2203 601-5276 (R. Anton).

Abstract

Mo-Si-Ti alloys show an improved oxidation behaviour at temperatures above 1000 °C compared to Mo-Si-B alloys by forming a SiO_2-TiO_2 oxide layer but at intermediate temperatures around 800 °C the major alloying element Mo still often leads to a catastrophic oxidation. Hence, Mo-Si-Ti alloys to be used at high temperature need a protective coating. In this study two coating systems were applied on the Mo-12.5Si-8.5B-27.5Ti-2Fe (at%) and the Mo-21Si-34Ti-0.5B alloy. The coefficient of thermal expansion of the alloys was analysed to be about 7.8×10^{-6} °C^{-1} at 1200 °C. The two coating systems consisted of a graded Mo-Si interlayer but differently sputtered Si top layers. The coating systems were investigated with respect to their deposition parameters, oxidation protection and interface reactions with the alloys. The coatings could protect the alloys successfully at 800 °C for 100 hours. At 1200 °C both coating systems evolved a thermally grown oxide SiO_2 forming a dense layer which can protect the alloys. At the interface between coating system and alloy an interdiffusion zone of mostly $(Mo,Ti)_5Si_3$ grew with increasing testing time.

Keywords: physical vapor deposition, silicon dioxide, titanium oxide, oxidation behavior, Mo-Si-Ti alloy, interdiffusion processes

1.Introduction

Mo-Si-B alloys are promising materials for future applications at high temperatures in gas turbines. However, they show poor oxidation resistance at intermediate temperatures around 600 – 800 °C. Once Mo forms MoO_3 the sublimation temperature of this oxide creates the so-called pesting phenomenon [1-4]. At temperatures above 1000 °C these alloys can form borosilicate but due to the slow growth rate a protective dense layer cannot be formed on the surface and therefore, still a massive weight loss through MoO_3 occurs. This behaviour is caused by mainly the Mo_{ss} and the Mo_3Si phases. Due to its ductility, the Mo_{ss} phase is still desirable within the alloy [5, 6]. In order to reduce the Mo_3Si phase content in such alloys, Yang et al. suggested macroalloying with Ti based on thermodynamic calculations. An amount of 27 to 29 at% Ti suppresses the Mo_3Si phase and supports the formation of $(Mo, Ti)_5Si_3$ in a Mo-12.5Si-8.5B alloy [7]. According to thermodynamic calculations, a new phase field of Mo_{ss}, Mo_5SiB_2 and Ti-rich Mo_5Si_3 causes the elimination of the Mo_3Si phase. Since the phase field is pretty narrow, the manufacturing is accompanied by substantial difficulties to inhibit the formation of the Mo_3Si phase completely. Further, Azim et al. predicted that the corresponding phase field could be broadened by alloying minor amounts of Fe [6]. The composition of the alloy predicted by thermodynamic modelling is Mo-12.5Si-8.5B-27.5Ti-2Fe (at%). Schliephake et al. found that the oxidation resistance of the Mo-12.5Si-8.5B-27.5Ti (at%) decreases at around 1100 – 1300 °C. This is due to the formation of a porous SiO_2/TiO_2 duplex oxide scale [8]. Therefore, developments of new Mo-Si-Ti alloys have been initiated. The $(Mo,Ti)_3Si$ phase on the Mo-rich side of the ternary Mo-Si-Ti phase diagram could be retrieved from the liquid by a congruent solidification. A eutectoid reaction triggers this phase to subsequently decompose into bcc (Mo, Ti, Si) and the tetragonal $(Mo, Ti)_5Si_3$ phase. In [9], an eutectoid alloy with the composition of Mo-21Si-34Ti (at%) was designed. A fine lamellar microstructure was obtained containing the phases (Mo, Si, Ti) solid solution and $(Mo, Ti)_5Si_3$. The alloy shows catastrophic oxidation around 800 °C and formation of a SiO_2/TiO_2 duplex

layer at temperatures around 1200 °C [9]. The Ti atoms exclusively substitute Mo-atoms on their respective lattice sites. Therefore, protective coatings for the newly developed Mo-Si-Ti-B-(Fe) alloys are mandatory. Moreover, improvements in the mechanical properties, a reduced density, and improved oxidation behaviour are initiated by changes in the alloy composition [6, 8, 9].

Protective coatings for Mo-Si-B alloys are studied intensely by using different deposition processes like pack-cementation, magnetron sputtering and dip coating where borosilicate or SiO_2 were mostly used as protective oxide and Mo-silicides and MoB formed between TGO and substrate [10-14]. But studies of coatings on the Mo-Si- Ti-(B)-(Fe) alloys described above are rare. Schliephake et al. [15] successfully improved the oxidation resistance by a co-pack cementation process on a Mo-12.5Si-8.5B-27.5Ti alloy. A Si-B coating was applied forming a Mo_5Si_3, $MoSi_2$ and a Ti_5Si_3 interlayer as well as a thermally grown oxide (TGO), i.e. borosilicate. The coating significantly enhanced the oxidation resistance at 800 to 1200 °C for up to 500 hours. Compared to the pack cementation used on the Mo-Si-B alloys, the Ti_5Si_3 layer can directly be linked to the Ti in the substrate [15]. Majumdar et al. investigated the oxidation behaviour at 1300 °C of the uncoated and coated alloys Mo-40Ti-10Si (at%) consisting of the phases $Mo(Ti)_{ss}$, $Mo(Ti)_3Si$ and $Ti(Mo)_{ss}$ as well as Mo-40Ti-30Si containing $Ti(Mo)_5Si_3$, $Ti(Mo)_3Si$ and $Mo(Ti)_{ss}$. Both alloys were siliconized via pack cementation which improved the oxidation resistance at 1300 °C due to protective silica scale. Compared to the studies on siliconized Mo-Si-B alloys, the Ti rich alloy triggered the development of different layers in the oxide scale and changed the oxidation behaviour considerably [16, 17].

A previous study on Mo-Si-B alloys showed that Si coatings manufactured by physical vapour deposition (PVD) can provide oxidation protection but tend to fail in further experiments due to a mismatch in the coefficient of thermal expansion (CTE) between coating and alloy [18]. A dual coating system containing a CTE matched Mo-Si graded interlayer and a Si top layer

showed better results [19]. Due to the high diffusion rate of Si in Mo by exposition in a vacuum atmosphere the crystallization treatment was done in lab air. The diffusion rate can be significantly slowed down by a post crystallization treatment in an oxidizing environment like lab air by the formation of the Mo_3Si phase found in [18] or by SiO_x [20]. Furthermore, the formation of pores on the surface of the Si top layer were found while applying a heat treatment in vacuum, which was not desirable. In addition, the crystallization in air helped to close the intercolumnar gaps rapidly due to SiO_2 formation. In the current work, the dual layer coating systems was implemented on the Mo-12.5Si-8.5B-27.5Ti-2Fe and on the Mo-21Si-34Ti-0.5B alloys and was tested in terms of their oxidation resistance. Since the alloys were fairly new within the field and the necessary compatibility between coating and alloy requires an evaluation of the CTE's, this was additionally executed in order to assess potential stress generation that would lead to cracks in the coating. By applying the same coatings as in [19] and a combination of [18, 19], that were investigated there on Ti-free alloys, the influence of Ti and Ti-Fe originating from the substrate on the oxidation behaviour can be determined.

2.Experimental

The substrate material was manufactured at the KIT. The manufacturing process was done in an arc melter (AM/0.5, Edmund Buehler GmbH) with a water-cooled copper crucible under Ar atmosphere. The Mo, Si, Ti, B and Fe materials were used in bulk form with purity of 99.95 %, 99.99 %, 99.8 %, 99 % and 99.98 %, respectively. The two alloys used in this study have compositions Mo-12.5Si-8.5B-27.5Ti-2Fe(at%) (3-phase) and Mo-21Si-34Ti-0.5B (2-phase). A subsequent heat treatment was done at 1600 °C for 150 hours following 100 hours at 1400 °C in Ar flow (3-phase) and 400 hours at 1300 °C in Ar flow (2-phase) in order to stabilize and homogenize the microstructure. The samples were wire cut in the dimensions of about 2 mm × 10 mm × 15 mm for the coating process. A different dimension of 10 mm × 8 mm × 8 mm was chosen to measure the CTE of the alloys itself. These samples have not been coated. Before coating or CTE measurements, the sample surface was firstly prepared

by a vibratory tumbler and secondly by grinding down until 1200 grid. Due to cutting and tumbling some of the edges got a more rounded shape while others had sharper edges which did not influence the results of this study. A commercially available alloy titan–zirconium–Mo (TZM) (Plansee AG, Reutte, Austria) with the nominal composition of Mo-0.5Ti-0.08Zr-0.01-0.04C was used for the analytical work in the as-coated condition during coating development. Due to its single-phase composition, the analysis could be focused on the coating systems without any interferences with the substrate.

In the present work, two different coating systems were applied on both alloys. The first coating system (CS1) is identical to the coating system investigated in [19] and was manufactured in a magnetron sputter facility (IMPAX, Systec SVS vacuum coatings, Karlstadt, Germany). The interlayer had a deposition rate of about 0.9 µm/h at a deposition temperature of 550 °C and bias voltage of -50 V. One Mo-Target and one Si target was used. The Si top layer of CS1 had a deposition rate of about 1.6 µm/h at a deposition temperature of 150 °C and a bias voltage of -100 V. The samples were rotated with a speed of 12 min^{-1} in front of one Si target. The second coating system (CS2) had the same interlayer but the Si top layer responsible for the oxidation protection was manufactured in a different coating machine (Z400, Systec SVS vacuum coatings, Karlstadt, Germany) while using different parameters. This machine was used because of its higher coating deposition rate due to a smaller target sample distance. The deposition rate of the Si top layer was about 3.3 µm/h, the deposition temperature was about 110 °C and the bias voltage was only -10 V. The samples were rotated with a speed of 10 min^{-1} in the middle of two Si targets. The parameters were described in detail in [18]. First experiments with a pure Si coating also used the parameter from [18] but did not incorporate an interlayer between the substrate and the top layer. Before coating, a wire was attached to all samples which functioned as the sample holder. Therefore, most of the surface was coated without any shading effects.

To determine the CTE, an optical dilatometer heating microscope (LINSEIS, Germany) was used. The above-mentioned cube-like samples were compared to an Al_2O_3 reference. The samples had an approximately 45° sharp edge aiming at detection of the length difference as compared to the reference using a CCD camera. The heating rate of 10 °C/min over the temperature range from 300 to 1200 °C under Ar flow of 3 sccm/min was chosen to analyse the CTE of the alloys.

Both coating systems were usually semi X-ray amorphous after deposition. Thus, a crystallization treatment is necessary and was carried out at 900 °C for one hour in air. No significant changes in morphology could be determined right after crystallization, therefore, no results will be shown in this paper. All samples were placed under lab air atmosphere in the already heated box furnace. Subsequently thereafter, oxidation tests were performed at 1200 °C for 10, 100 and 300 hours. To proof the pest phenomenon resistance, oxidation experiments were also performed in lab air at 800 °C for 100 hours, ramping the furnace down directly after crystallization. To evaluate the oxidation resistance of the coatings, uncoated samples were also tested under the same conditions. Mass changes were documented with a micro weight scale ME5-OCE (Sartorius, Germany) before and after the oxidation tests to determine the oxidation rates depending on the time of exposure at 1200 °C.

Various analytical methods were used. X-ray diffraction (XRD) (Bruker D8 Advance, Cu K_α radiation, EVA/Topas 4.2 software package, Bruker AXS, Karlsruhe, Germany) revealed the phases and the phase changes throughout the experiments. The morphology was analysed by using a scanning electron microscope (SEM) (DSM Ultra 55, Carl Zeiss NTS, Wetzlar, Germany) with a voltage of 5 kV. Energy dispersive X-ray spectroscopy (EDS) system (Aztec, Oxford Instruments, Abingdon, UK) could support the XRD results and was used at 15 kV. Two lamellae were prepared after testing for 300 h at 1200 °C by a focused ion beam (FIB) (Dual Beam FEI Helios, FEI Philips, The Netherlands). Afterwards, the lamellae were analysed

in a transmission electron microscopy (TEM) at University of Siegen. Scanning transmission electron microscopy (STEM) EDS analyses and electron diffraction measurements applying selected area diffraction (SAD) (Talos F200 kV FEI, The Netherlands) were performed.

3.Results

3.1.Development of a CTE matched coating system

In order to develop a low stress creating oxidation protective coating for the 3-phase and 2-phase alloy, the CTEs were measured. Fig. 1 a) shows the CTEs depending on the temperature from 400 °C to 1200 °C. The alloys show very similar curves. The 3-phase alloy yielded a CTE being about 7.2 × 10^{-6} °C^{-1} (at 400 °C) to 7.7 × 10^{-6} °C^{-1} (at 1200 °C) while the 2-phase alloy exhibits values raising from 7.2 × 10^{-6} °C^{-1} (at 400 °C) to 7.8 × 10^{-6} °C^{-1} (at 1200 °C). In Fig. 1 b), the microstructure of the 3-phase alloy is shown with the three distinguished phases of Mo_{ss} (light), $(Mo,Ti)_5Si_3$ (middle grey) and Mo_5SiB_2 (dark grey). The 2-phase alloy shown in Fig. 1 c) presents a fine-grained eutectoid microstructure of $(Mo,Ti)_5Si_3$ (dark) imbedded in a $(Mo,Ti)_{ss}$ (light) matrix. For a detailed description of the microstructure of both alloys see references [8, 9].

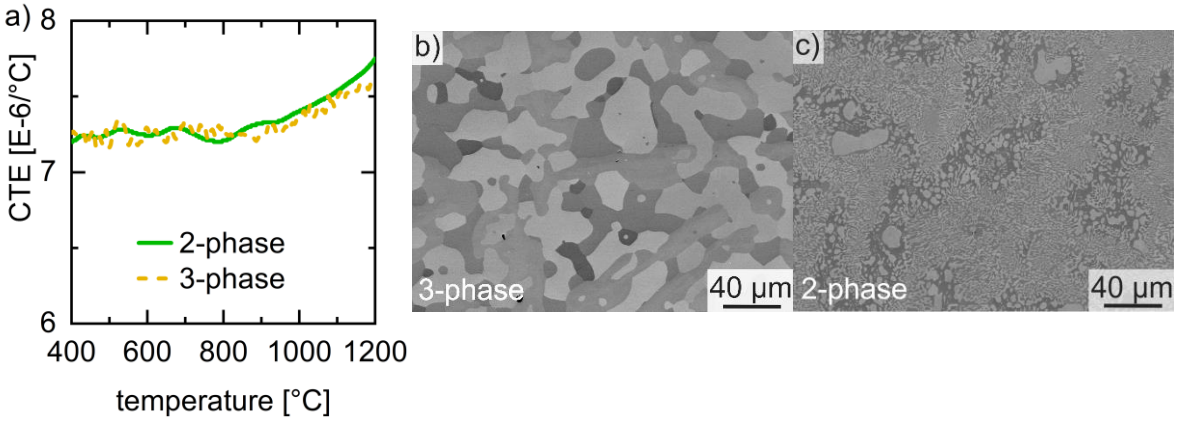

Fig. 1 a) CTE versus temperature of the 3-phase and 2-phase alloy; secondary electron SEM cross-sectional micrographs of the microstructure of the manufactured 3-phase alloy b); the 2-phase alloy c).

First coating deposition trials on the 3-phase alloy and the 2-phase alloy are shown in Fig. 2. A pure Si coating was applied by using the lab coater (Z400), which was found to be promising

as an oxidation protection layer on a Mo-9Si-8B alloy [7]. Unfortunately, failure of the coating due to crack initiations occurred on both alloys after 100 h of exposure at 1200 °C in air. The spallation of the coating in large areas is followed by the oxidation of the substrate alloys forming SiO_2 with imbedded TiO_2 along the surface as well as the interface between substrate and coating (Fig. 2 a), b)). In parts where the coating is still present, the cracks are filled with mixed oxides (SiO_2 with embedded TiO_2) which also continue to grow on the surface of the coating. At the surface of the coating, TiO_2 forms a bridge-like grain (Fig. 2 b)). In regions away from the cracks, the coating developed a TGO SiO_2 layer. This clearly demonstrates the necessity of a CTE matched interlaced which is described below.

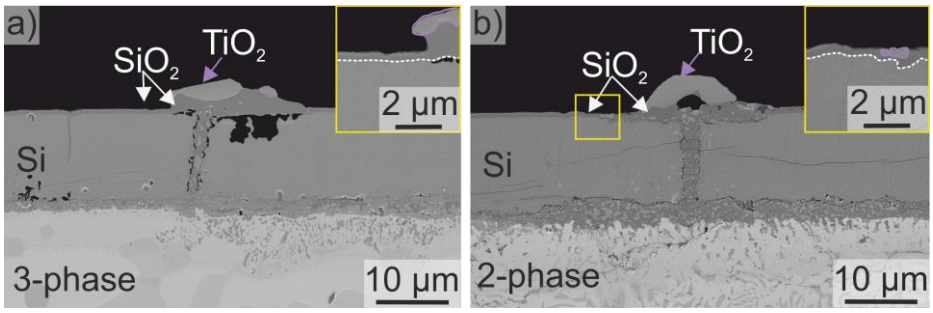

Fig. 2 Secondary electron SEM cross-sectional micrographs of a pure Si coating a) deposited on the 3-phase alloy with a close up of the TGO and b) deposited on the 2-phase alloy with a close up of the TGO; both after 100 hours of isothermal exposure at 1200 °C in laboratory air.

3.2.Coating systems with graded Mo-Si interlayer in the as-coated state

Fig. 3 displays the as-coated CS1 and CS2 on a TZM substrate. Similar to the CS1 from [19], a dense structure can be seen when looking at the Mo-Si interlayer in the area of the interface to the base material in Fig. 3 a) where the polished cross section is displayed. With increasing layer thickness, the formation of a columnar structure is recognizable in the interlayer. The individual columns show a certain growth direction and no ideal vertical growth with respect to the substrate surface. Columnar gaps form in the upper interlayer region. The Si top layer of CS2 grew on the interlayer as well as on the columnar gaps (Fig. 3 b)). However, compared to the Si top layer of CS1, the inter-columnar gaps in the CS2 are wider and predominantly

continue up to the surface. In CS2, the columns can be clearly determined in the Si top layer while CS1 shows a denser Si layer, Fig. 3 a) and b). The morphology of CS2 shows a coarser surface texture than CS1. The EDS line scan profile of CS2 (see Fig. 3 c) displays an increase in the Si concentration within the Mo-Si interlayer with increasing layer thickness, while the Mo concentration remains constant. Since the power control of the Mo target which was successively reduced, the Mo concentration should decrease. This effect is not shown within the linescan since oxygen is displayed here as well. Oxygen can be measured within the lower part of the interlayer while the top layer shows no oxygen (Fig. 3 c)). The oxygen-rich phases are darker within the SEM micrograph in Fig. 3 c). No argon can be measured in the Si top layer of CS2 (Fig. 3 c)) which is in contrast to CS1 where up to 1 at% Ar has been detected [19].

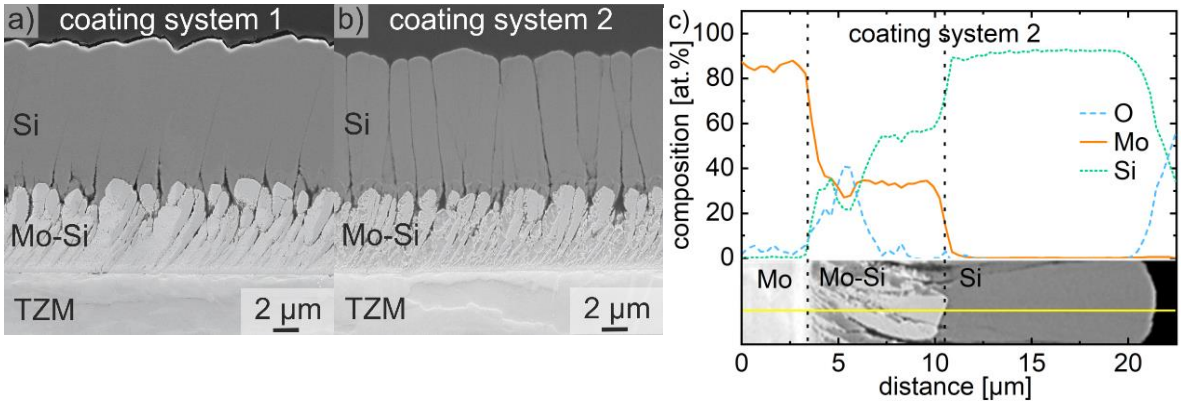

Fig. 3 Secondary electron SEM cross-sectional micrographs of the cross section of the dual coating system after deposition by magnetron sputtering, a) CS1 b) CS2 c) CS2 with EDS line scan in at%, deposited on a TZM substrate.

3.3.Oxidation kinetics of the coating systems 1 and 2

Weight change measurements were performed in laboratory air for 10, 100 and 300 hours at 1200 °C. The mass change curves of the uncoated and coated substrate alloys are shown in Fig. 4 a) during the isothermal oxidation tests at 1200 °C in air. The uncoated 3-phase alloy has a maximal mass loss of approx. 15 % and also exhibits no significant further weight changes after 100 hours. The uncoated 2-phase alloy exhibits a weight loss of approx. 0.85 % after

300 hours of oxidation. The weight change curves for the CS1 on the 2-phase and 3-phase substrates are almost constant over 300 hours. The 2-phase coated substrate initially experiences a weight loss of approx. 0.2 % up to an oxidation of 100 hours. Subsequently, a weight increase takes place, so that after 300 hours, a weight loss of approx. 0.1 % results compared to the initial state. With respect to the uncoated 2-phase substrate material, the mass loss can be reduced by about 88 % if CS1 is applied. For the CS1-coated 3-phase alloy, only marginal mass changes are identifiable compared to the initial state. Thus, after 300 hours of oxidation, there is a weight increase of only 0.02 %.

The weight change curves of the 2-phase and 3-phase alloys coated with CS2 during oxidation at 1200 °C follow a different behaviour than those recorded during oxidation of CS1-coated alloys. Both curves initially show no significant weight changes up to 100 hours. However, up to an oxidation of 300 hours, the weight decreases by approx. 17 % for the coated 2-phase sample, thereby having a greater mass loss than the uncoated alloy which is quite stable. In the opposite direction, the coated 3-phase alloy increases its weight by approx. 14 % (Fig. 4 a)). Compared to the CS2, the samples of CS1 showed only a minor weight reduction of 0.1 % for the 2-phase alloy and a mass increase of 0.02 % for the 3-phase alloy after 300 hours of oxidation.

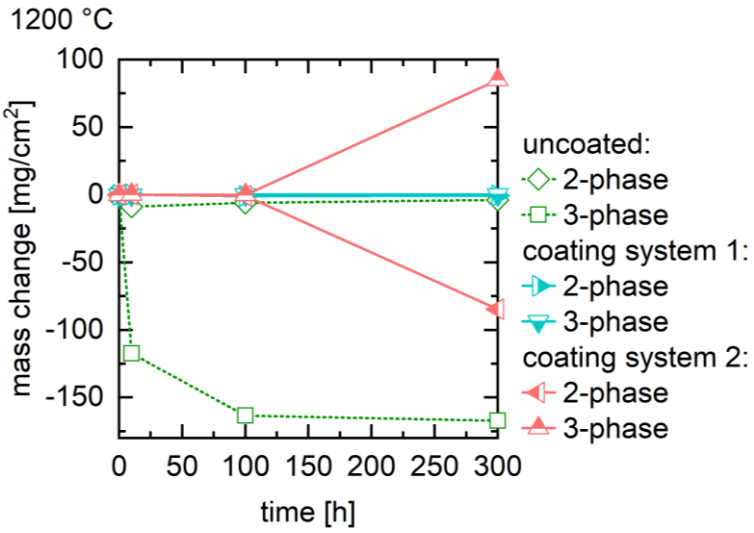

Fig. 4 Mass change versus time during isothermal testing at 1200 °C until 300 hours of 3-phase alloy and 2-phase alloy (uncoated, with CS1 and with CS2).

The macroscopic images of the specimens help to understand and support the weight curves explained above. Fig. 5 shows the uncoated alloys after 300 h of oxidation as well as the CS1 samples. The uncoated 3-phase alloy has an oxidised dark grey surface but maintains still its original shape. The coated 3-phase alloys in Fig. 5 experience small spallation on the edges. Furthermore, starting at 100 hours a yellow-brownish discoloration of the coating surface can be seen, which clearly spreads and increases in intensity with increasing oxidation. As far as can be seen from the SEM micrographs, the adhesion of the coating is not affected.

The uncoated 2-phase alloy in Fig. 5 inhibits also its original shape but reveals an oxidized surface with light and dark grey as well as yellow. The yellow colour could proof some pest oxidation processes forming MoO_3 [21]. The coated 2-phase alloy after 10 hours shows no sign of disruption. After removal from the high-temperature furnace, large-area spalling of the layer can be seen in the samples that were aged for 100 and 300 hours. The failure always occurred in the area of the oxide phase between the Mo-Si interlayer and the Si top layer which leads to the detachment of the complete Si layer including the TGO, as proven in a later section by SEM (Fig. 11 b)). The remaining layer segment, the interlayer, continues to show good adhesion to the base material. Surprisingly, the edge areas are almost completely excluded from the spallation of CS1 which mostly happened in the middle regions of the surface.

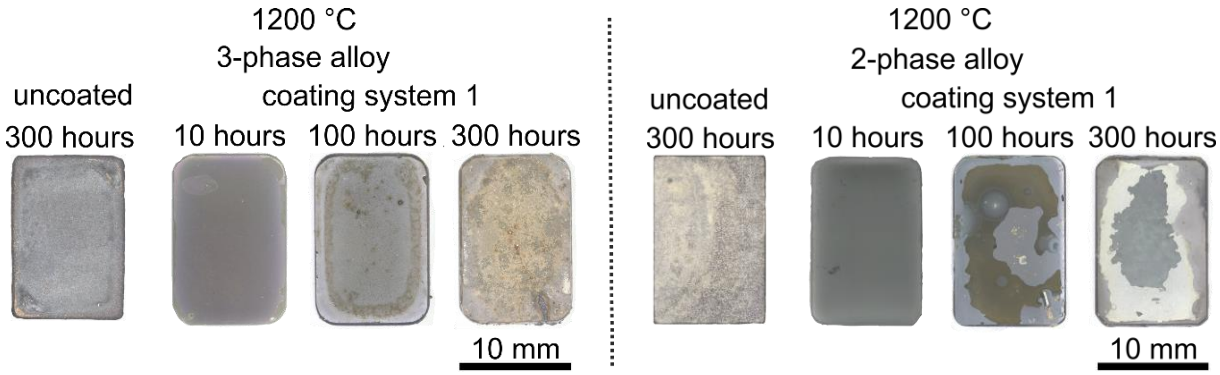

Fig. 5 CS1 macro images of the at 1200 °C isothermal tested uncoated and coated 3-phase alloy as well as the uncoated and coated 2-phase alloy.

The CS2 applied on the 3-phase sample shows a red-pink discoloration of the coating surface macroscopically after 10 hours oxidation (Fig. 6). After 100 hours, a red-brownish discoloration is initially visible, which increases in intensity after 300 hours and finally appears yellow-brownish. The adhesion of the coating is very good since macroscopic spallation of the layers was not found.

The 2-phase coated alloy shows as well as a macroscopic red-pink discoloration of the surface after 10 hours of oxidation (Fig. 6). Already after 100 hours, large-area layer spalling can be seen in the edge region. The same applies to oxidation of 300 hours. While coating spallation was similarly observed for the CS1 on the 2-phase alloy, the failure seems to initiate for CS2 from the edges which is a distinct difference. The failure of the layer becomes apparent after removal of the specimens from the high-temperature furnace which was seen for CS1 as well.

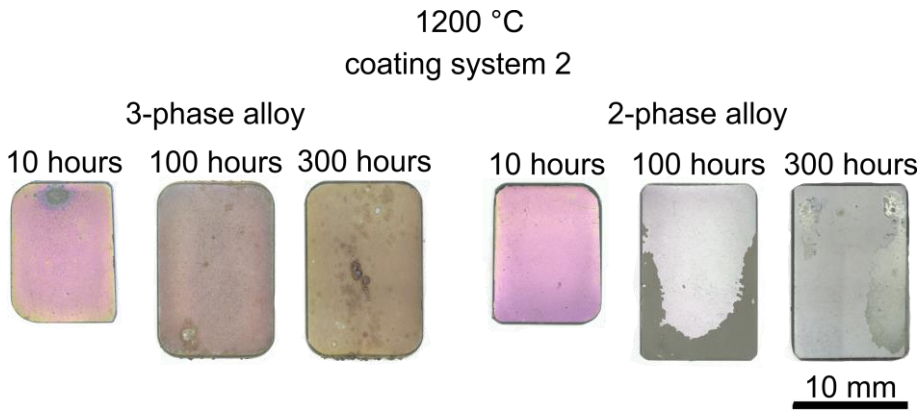

Fig. 6 CS2 macro images of the isothermal tested coated 3-phase alloy and coated 2-phase alloy.

In addition to the weight measurements, the growth of the TGO at the coating surface is crucial for a successful oxidation protective coating. The diagram of Fig. 7 shows the outer SiO_2 TGO thickness with increasing testing time at 1200 °C measured for every pixel distance within the SEM micrographs by the help of ImageJ. The SiO_2 TGO is growing on top of the Si top layer and preserves the substrate from oxidation. Until 100 hours, CS2 shows a thinner TGO compared to CS1 (Fig. 7). After 300 hours of testing time the TGO of all coatings lies between 1.68 µm until 1.86 µm. Note that for coatings that have partially spalled only the intact regions have been considered for these measurements. The TGOs follow a parabolic growth rate which is described by the black dotted line as expected. Overall, the differences in TGO thicknesses of the Si top layer are small when both coatings on both alloys are compared.

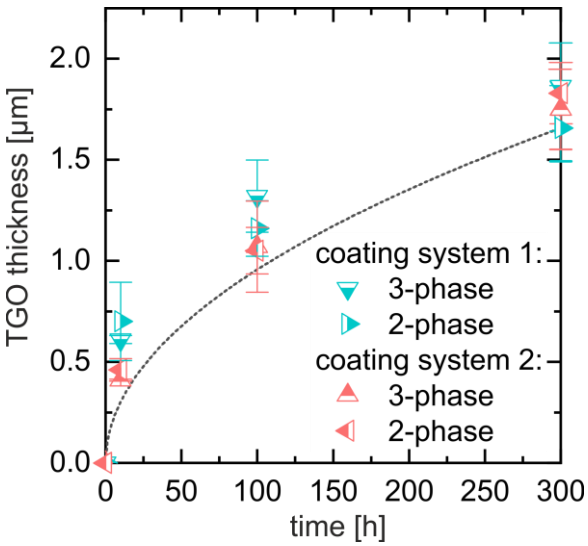

Fig. 7 SiO_2 TGO growth depending on the isothermal exposure time of the CS1 and CS2 deposited on the 3-phase and 2-phase alloy with a parabolic trendline at 1200°C in laboratory air.

In Fig. 8 a) and b), the 3-phase and 2-phase alloys were presented after 300 hours oxidation at 1200 °C. The 3-phase alloy showed almost a complete degradation of the original substrate. The 2-phase alloy formed a about 100 µm TiO_2-SiO_2 mixed oxide scale accompanied 100 µm internal oxidation.

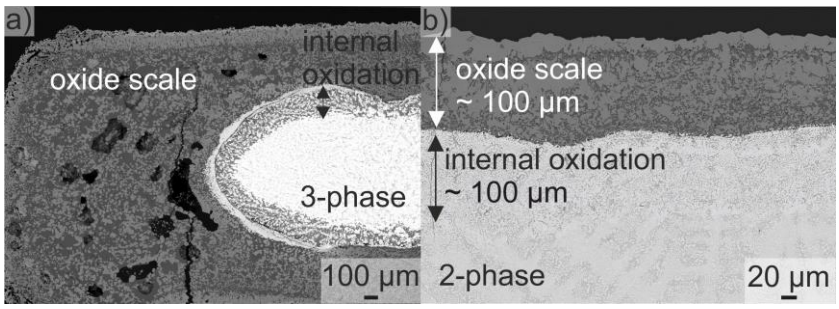

Fig. 8 Secondary electron SEM cross-sectional micrograph a) of the uncoated 3-phase alloy; b) of the uncoated 2-phase alloy after 300 hours at 1200 °C.

To proof the pest phenomenon resistance coatings were tested until 100 hours at 800 °C in laboratory air. Fig. 9 a) shows an overview diagram comparing the uncoated and coated substrate. The uncoated 2-phase and 3-phase alloys show a massive decrease in weight caused by pest oxidation. Thus, the mass loss is even bigger than at 1200 °C. The testing at intermediate temperature is therefore very crucial for the assessment of the overall behaviour of the alloys and coatings. Fig. 9 b) displays the macro images of the samples after testing. The massive pest oxidation of the 3-phase alloy leads to a red coloured surface due to the oxidized Fe and to massive cracks. Furthermore, the 2-phase alloy has a yellow and white surface due to MoO_3 and a puff pastry like structure which makes the sample fall apart. The coated alloys are all intact and are almost not distinguishable with only small mass losses between 0.05 % (CS1 on 2-phase) and 1.4 % (CS2 on 3-phase), see Fig. 9 a). The macro images support the finding by showing no spallation or changes except for the blue colour. The bigger mass loss of the 3-phase alloy with CS2 after 100 hours is also not caused by coating failure but rather because of a slightly larger uncoated area where the wire necessary for holding the sample during coating deposition was attached on the surface of the sample. A massive growth of oxides could be found there which is displayed by the macro image in Fig. 9 b). The SEM analyses of the cross sections of the coating systems displayed well adherent coatings with a microstructure similar to the as-coated conditions as shown in Fig. 3 a) and b). Only a slight formation of SiO_2 along the intercolumnar gaps as well as on top of the Si top layer coating was found. Therefore, SEM micrographs after testing at 800 °C are not shown here.

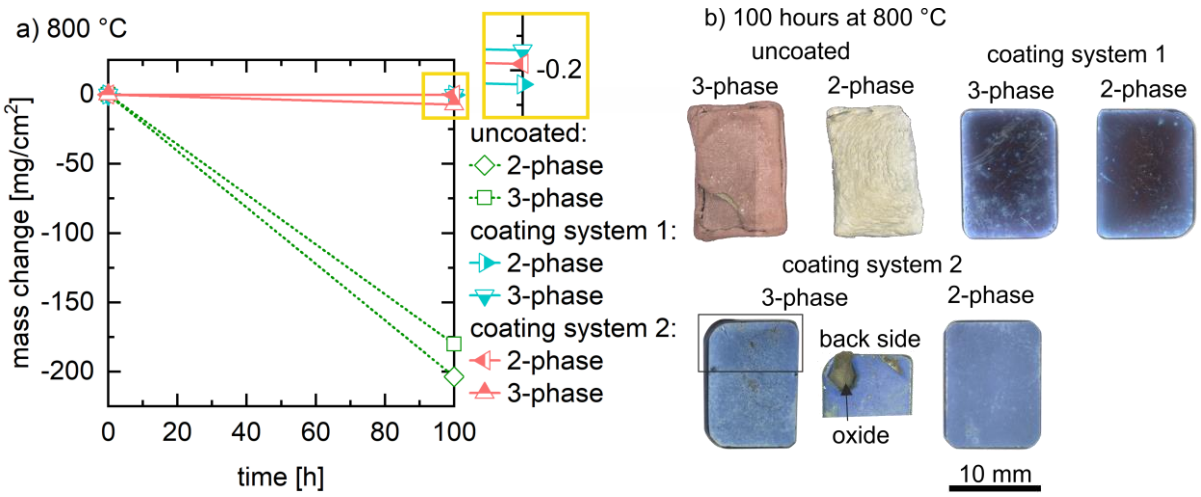

Fig. 9 a) Mass change versus time during isothermal testing at 800 °C until 100 hours of 3-phase alloy and 2-phase alloy uncoated, with CS1 and with CS2; b) Macro images of the 3-phase and 2-phase alloy isothermal tested at 800 °C for 100 hours uncoated, with CS1 and with CS2.

3.4.Microstructural analysis of the coating systems on the 3-phase and the 2-phase alloy during oxidation testing

3.4.1.Coating system 1

In the following, the results of the microstructure of CS1 deposited on the 3-phase alloy are presented. After 10 hours at 1200 °C (Fig. 10 a)), porosity can be seen within the Si top layer of the 3-phase alloy. With increasing oxidation, no crucial increase but an agglomeration of the pores can be observed. The Mo-Si interlayer itself shows a breakdown of the columnar structure compared to the as-coated state. According to EDS analysis the interlayer consists of 45 at% Mo, 35 at% Si and approx. 15 at% Ti after 10 hours. Already in this state, SiO_2 has formed in the former columnar interstices. After an oxidation of 100 hours (Fig. 10 b)), a SiO_2 phase is formed at the interface between interlayer and top layer. The former columnar microstructure of the interlayer has nearly fully disappeared so that this layer is now more homogeneous (Fig. 10 b)). In the interface between the Mo-Si interlayer and the SiO_2 phase, TiO_2 can be detected. These oxides continue to form at an oxidation of 300 hours (Fig. 10 c)). Moreover after 300 hours, the pores are largely concentrated in the area above the interlayer (Fig. 10 c)). The upper TGO consists of a dense layer of silica that is slightly undulated. Already after 100 hours shown in Fig. 10 b), bright spherical precipitates which are mostly not connected can be

seen within the TGO layer. There number has clearly increased in the upper area of the TGO after 300 hours (Fig. 10 d)). They are following a horizontal line along the TGO. According to the EDS analyses in Fig. 10 e), Fe oxide can be identified in those precipitates.

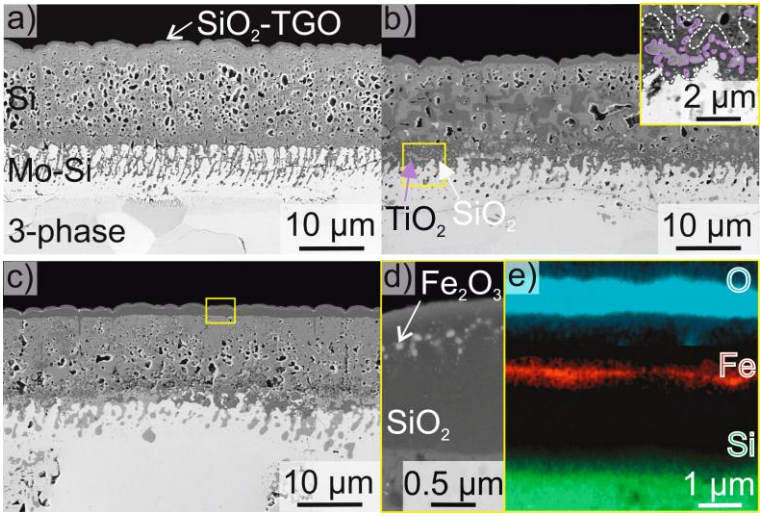

Fig. 10 Secondary electron SEM cross-sectional micrographs of the CS1 deposited on 3-phase alloy, after a) 10 hours, b) 100 hours with a close up of the interface and c) 300 hours, d) close up of TGO; e) EDS mapping of TGO in at% after 300 hours of isothermal exposure to 1200 °C in laboratory air.

Fig. 11 a)-c) depicts the evolution of CS1 on the 2-phase alloy. As with the 3-phase alloy, after 10 hours, the Si top layer develops pores and a TGO layer of SiO_2. The Mo-Si interlayer columns are surrounded by Si as well as SiO_2 (Fig. 11 a)). After 100 hours of oxidation (Fig. 11 b)), a clearly increased micro-porosity can be seen, which extends through the entire Si top layer. The Mo-containing microstructure of the Mo-Si interlayer shows a reduction of the column width as well as a clear irregularity of the columnar structure. The columnar structure of the interlayer starts to break down and to transform into a more homogeneous layer, similarly to the behaviour on the 3-phase alloy described above. After 100 hours a clearly separated region between interlayer and top layer and above the Mo-Si interlayer evolves (Fig. 11 b)). It contains SiO_2 with TiO_2 particles embedded and has a thickness of approximately 3 µm. This phase mixture fills also the remaining inter-columnar areas of the former upper interlayer. After 300 hours, the SiO_2 continues to growth into the Si top layer,

oxidizing the coating from inside. Simultaneously the top TGO increases in thickness as well. Only the upper half of the Si top layer still remains not oxidized (Fig. 11 c)).

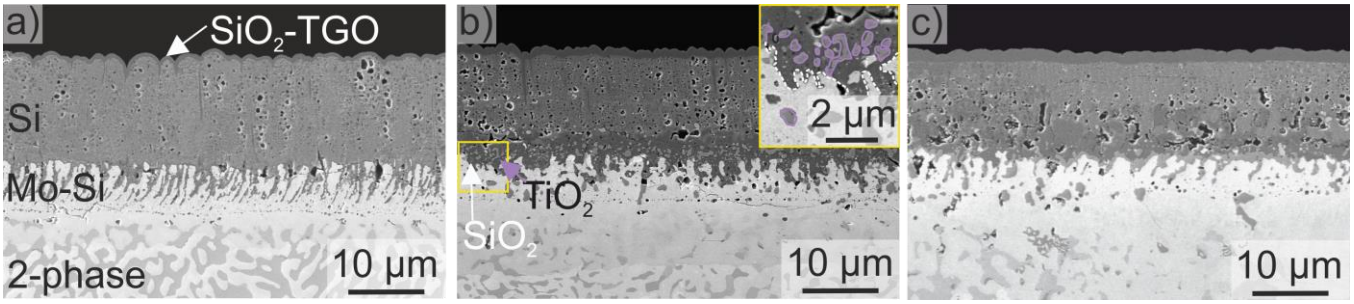

Fig. 11 Secondary electron SEM cross-sectional micrographs of the CS1 deposited on 2-phase alloy, after a) 10 hours, b) 100 hours with a close up of the interface and c) 300 hours of isothermal exposure to 1200 °C in laboratory air.

In order to identify the phases, XRD scans of the CS1 with the 3-phase alloy as substrate material is represented in Fig. 12 a). On the one hand, the intensities of the Si peak as well as the $MoSi_2$ and Mo_5Si_3 peaks decrease with increasing testing time from 10 hours to 300 hours. On the other hand, the SiO_2 peaks increase reciprocally following the TGO development. Small peaks of Fe oxide can be found already after 100 hours of isothermal heat treatment which agrees with the SEM micrographs and confirms the development of Fe_2O_3 as bright precipitates in the TGO (see Fig. 10 c)-e)). TiO_2 could also be identified but mostly in small peaks which are not visible here due to the low intensity.The diffractogram of the layer deposited on the 2-phase substrate (Fig. 12 b)) is very similar to that of the 3-phase alloy after 10 hours oxidation. After 100 hours of testing, an increase in intensity of the Mo_5Si_3 peaks can be observed, whereas the Si peaks are reduced to a minimum. Moreover, the $MoSi_2$ peaks disappear almost completely but small TiO_2 peaks are identified. After 300 hours of oxidation, a significantly increased intensity of the SiO_2 peaks can be seen. In addition, a reduction of the Mo_5Si_3 peaks can be seen both in comparison to the XRD scan of the samples after 10 hours and after 100 hours.

The XRD scans of the CS2 (not shown here), applied to the 3-phase alloy show a behaviour analogous to the previous diffractograms of CS1. The Fe oxide peaks are also visible after

already after 100 hours. CS2 deposited on the 2-phase alloy is also almost identical to Fig. 12 b) and is therefore not displayed here.

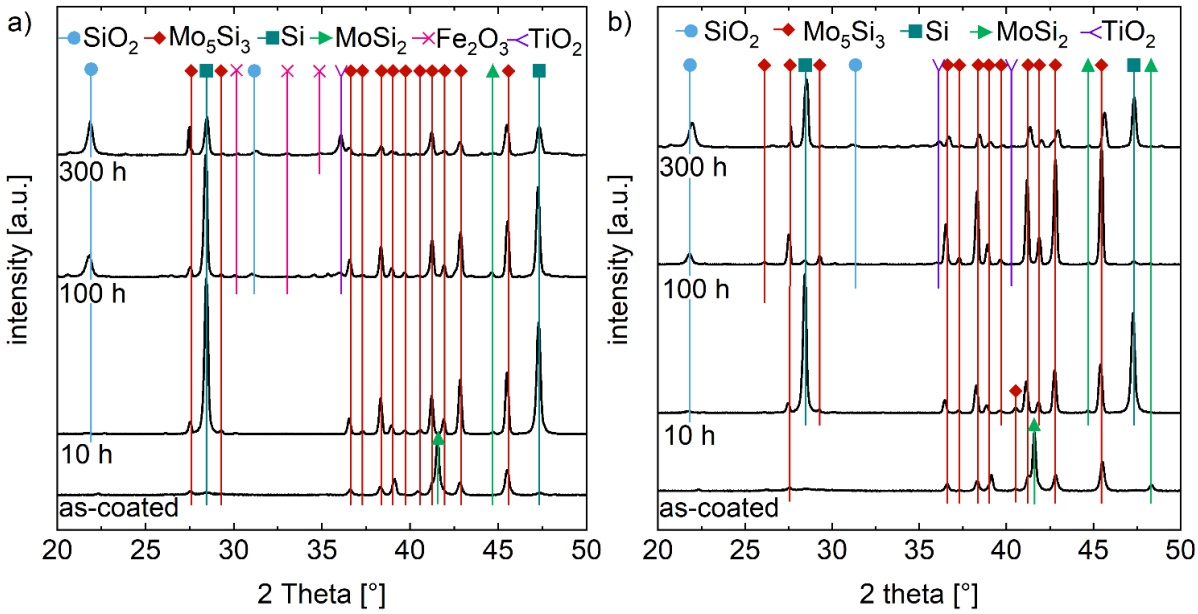

Fig. 12 XRD scans of the CS1, deposited on a) 3-phase alloy in as-coated state, after 10, 100 and 300 hours, and deposited on b) 2-phase alloy in as-coated state, after 10, 100 and 300 hours isothermal exposure time at 1200 °C in laboratory air.

With increasing oxidation time, the growing of an interdiffusion zone (IDZ) in the subsurface area of the two substrate materials can be identified (Fig. 13). The interdiffusion zone formed within the 3-phase alloy increases in thickness from approx. 3.5 µm after 10 hours (Fig. 13 a)) to 7 µm after 100 hours (Fig. 13 b)), ending at a thickness of 10.8 µm after 300 hours (Fig. 13 c)). Even though Si diffuses into the substrate, the original phases are still visibly distinguishable due to intensity contrast after 10 hours in Fig. 13 a). After 100 hours and 300 hours the IDZ develops a more homogenous zone with some internal oxidation replacing the original morphology of the substrate.

The IDZ of the 2-phase alloy with CS1 is also documented in Fig. 13. EDS analyses detected an enrichment of Si in this region up to a concentration of about 38 at%. The same observation as with the 3-phase alloy can be seen here. After 10 hours in Fig. 13 d) the Mo_{ss}/Ti_{ss} phase (light grey) as well as in the $(Mo,Ti)_5Si_3$ phase (dark grey) are still visible with the IDZ. With

increasing testing time shown in Fig. 13 e) and f) the IDZ again becomes more homogenous. Compared to the samples of the 3-phase alloy, the interdiffusion zone of the 2-phase alloy extends over a significantly larger thickness. After 10 hours of oxidation (Fig. 13 d)), the interdiffusion zone already has a thickness of about 4.2 µm. After 300 hours of oxidation, this increases to a maximum thickness of approx. 14 µm (Fig. 13 f)) and is thus larger than the IDZ of the 3-phase alloy sample.

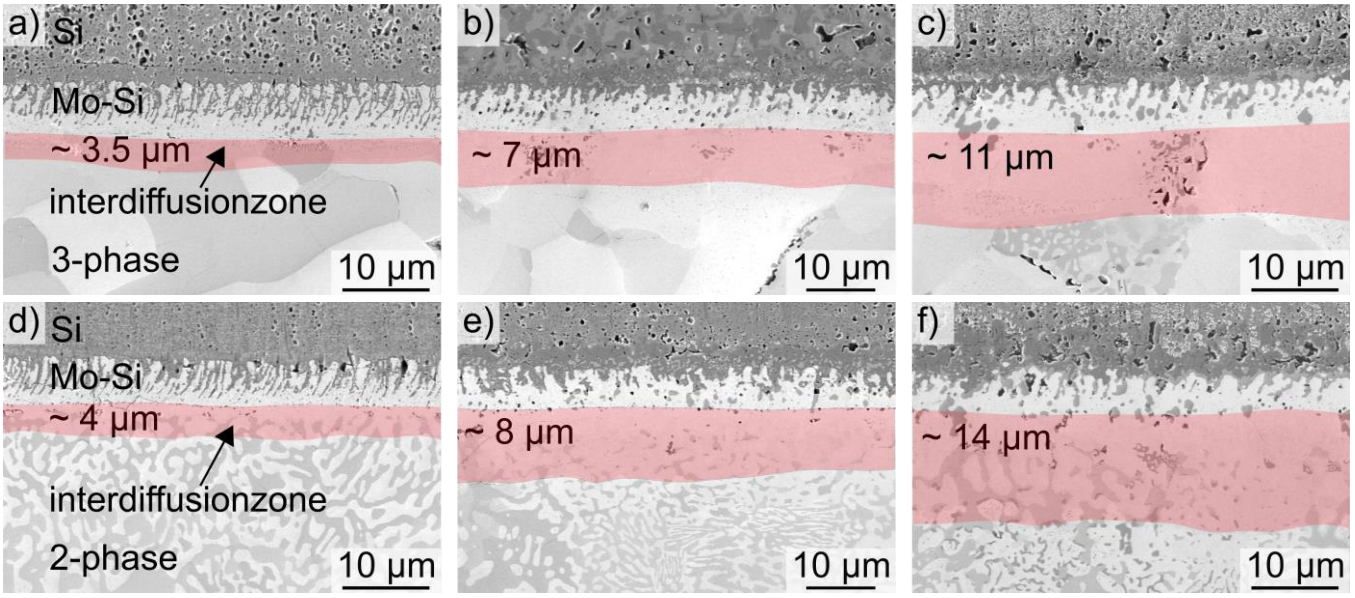

Fig. 13 Secondary electron SEM cross-sectional micrographs showing the CS1 evolution of the interdiffusion zone, deposited on 3-phase alloy, after a) 10, b) 100 and c) 300 hours, and deposited on 2-phase alloy, after d) 10, e) 100 and f) 300 hours isothermal exposure time at 1200 °C in laboratory air. For better visibility, the IDZ is marked by a light red colour band.

In order to analyse the intermetallic phases in the IDZ of the 3-phase and 2-phase alloy, TEM investigations were carried out. Fig. 14 shows the FIB lamella of the coated 3-phase alloy after 300 hrs of exposure to 1200 °C. The overview micrograph contains both IDZ and the lower part of the interlayer (Fig. 14 a)). An EDS mapping of this region shown here reveals a uniform distribution of Si (Fig. 14 c)). The border of IDZ can be determined by the Ti (Fig. 14 d)) and Mo (Fig. 14 b)) mapping image due to an intensity change within the IDZ compared to the interlayer. The mapping of oxygen and Ti (Fig. 14 e) and d)) together with diffraction analyses of single grains reveal them to be TiO_2 rutile (ICSD 9161) within the whole region shown here.

The diffraction of different grains suggests that the predominate phase within the interlayer is Mo_5Si_3 (ICSB 35756). The IDZ seems to consist of $(Mo,Ti)_5Si_3$ taking the EDS mapping as well as the diffraction in (Fig. 14 f)) into account.

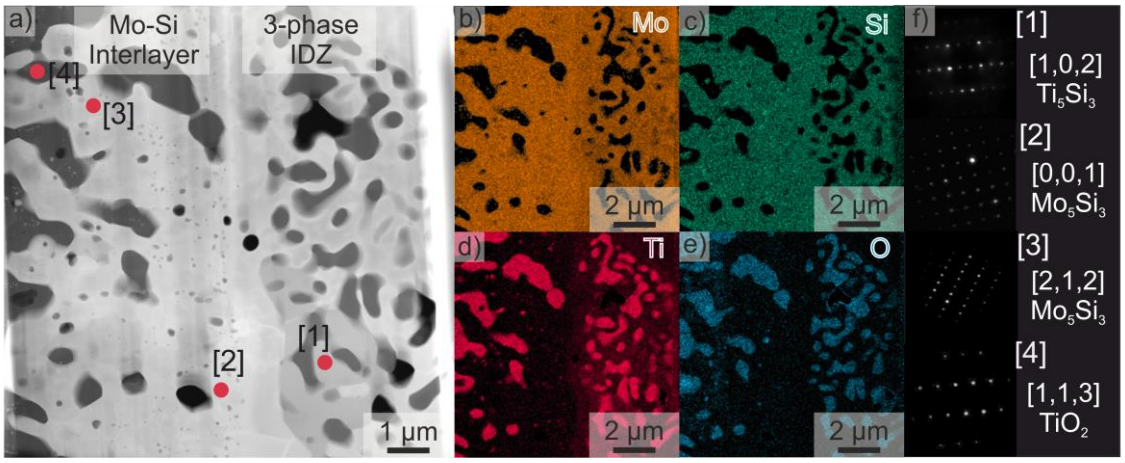

Fig. 14 TEM analyses of the coated 3-phase alloy after 300 hours of oxidation at 1200 °C; a) HAADF STEM of the 3-phase IDZ and Mo-Si interlayer; b) – e) EDS element mappings showing the Mo, Si, Ti and O parts in at%; f) SAED pattern and crystal plane of the in a) marked grains.

For the 2-phase coated alloy, a lamella was prepared as well after 300 h testing at 1200 °C (Fig. 15 a)). Again, the focus was put on the IDZ rather than on the Si top layer. The lamella shows SiO_2 in the interlayer which has been already pointed out in Fig. 13 f). TiO_2 is also present in some grains within the upper interlayer. Following the interlayer inwards no clear line can be drawn between IDZ and substrate materials. The mappings of Mo, Si and Ti (Fig. 15 b), c), d)) show no change in intensity within the IDZ. Furthermore, no oxide phases can be found within this area of IDZ/substrate (Fig. 15 e)). The analysed phases are Mo_5Si_3 (ICSB 35756) and $(Mo,Ti)_3Si_5$ (ICSB 35756),taken the EDS data into account, within the interlayer as well as Ti_5Si_3 (ICSD 44386) or possibly even $(Ti,Mo)_5Si_3$ (Fig. 15 f)).

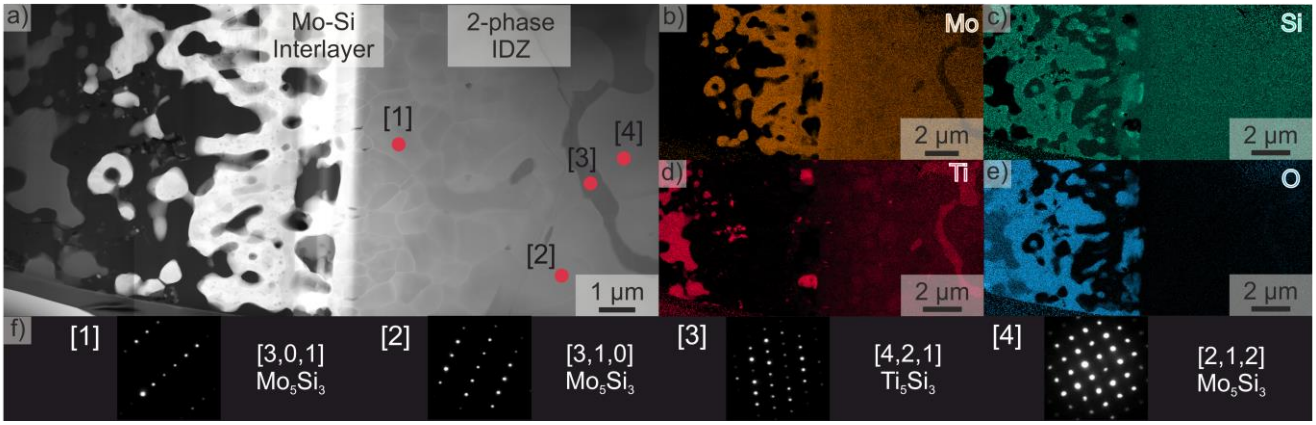

Fig. 15 TEM analyses of the coated 2-phase alloy after 300 hours of oxidation at 1200 °C; a) HAADF STEM of the 2-phase IDZ and Mo-Si interlayer; b) – e) EDS element mappings showing the Mo, Si, Ti and O parts in at%; f) SAED pattern and crystal planes of the in a) marked grains.

3.4.2. Coating system 2

Fig. 16 shows the cross-section sections of CS2, deposited on the 3-phase alloy after oxidation tests at 1200 °C. After 10 hours of exposure a thin, dense TGO of SiO_2 was developed providing a good oxidation protection on both alloys. The interfaces between both substrate alloys and the Mo-Si interlayer, as well as between interlayer and Si coating provide an excellent adhesion up to the maximal tested time of 300 hours.

In Fig. 16 a) and b) the formation of the SiO_2 between the columns, in the area of the former inter-columnar gaps, is concentrated in the area above the interlayer within the Si layer as well as in the upper part of the formerly columnar interlayer. As already in the previous presented CS1, the breakdown of the columnar interlayer structure can be seen after only 10 hours of oxidation. After 100 hours, EDS analyses (not shown here) reveals the formation of isolated TiO_2 grains at the interface between Mo-Si interlayer and Si top layer in Fig. 16 b). The concentration of these oxides of SiO_2 and TiO_2 within the interlayer increases significantly around 300 hours (Fig. 16 c)). In Fig. 16 d), CS2 deposited on the 3-phase alloy also shows light particles within the TGO layer. The EDS map also identifies them as Fe oxide (Fig. 16 e)). The close up in Fig. 16 d) shows that the particles are located in the upper half of the TGO as a nearly continuous layer closer to the surface.

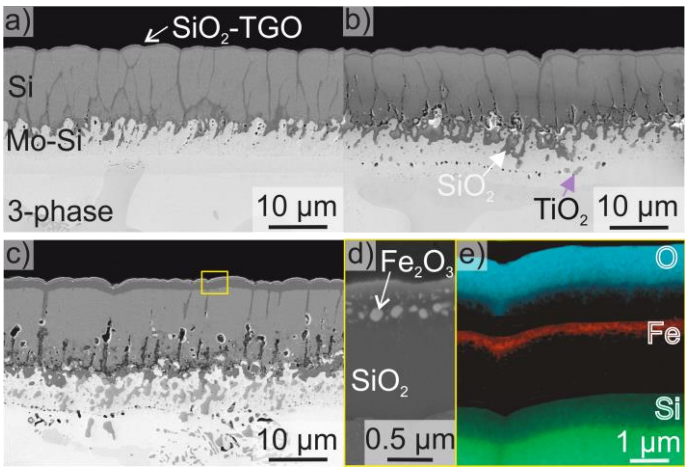

Fig. 16 Secondary electron SEM cross-sectional micrographs of the CS2 deposited on 3-phase alloy, after a) 10, b) 100 and c) 300 hours; d) close up of TGO; e) EDS mapping of TGO in at% after 300 hours of isothermal exposure at 1200 °C in laboratory air.

After 10 hours, the CS2 on the 2-phase alloy formed SiO_2 in the columnar interstices of the interlayer and within the Si top layer (Fig. 17 a)). As seen before, an SiO_2 layer between top layer and interlayer starts to develop with TiO_2 in between after 100 hours of testing (Fig. 17 b)). The growth of the oxide scale as TGO on top and as intermediate layer between top layer and interlayer continues further up to 300 hours (Fig. 17 c)). The morphology of the interlayer changes significantly showing no columnar structures anymore. Within the interlayer, island-shaped regions of TiO_2 and some Mo oxides are detected in addition to the SiO_2 phase (Fig. 17 c)). In the area of the intermediate SiO_2 layer, pores can be observed while the Si top layer remains pore free.

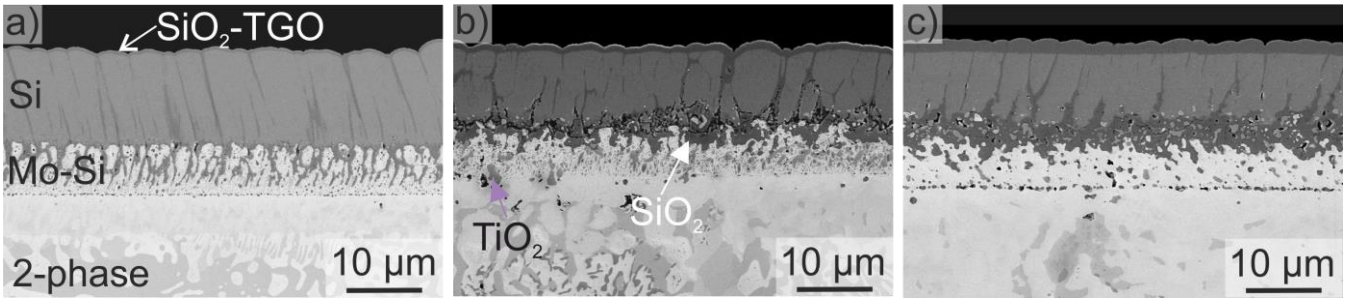

Fig. 17 Secondary electron SEM cross-sectional micrographs of the CS2 deposited on 2-phase alloy, after a) 10, b) 100 and c) 300 hours of isothermal exposure at 1200 °C in laboratory air.

As can be seen in Fig. 16 and Fig. 17, the CS2 develops a growing interdiffusion zone with increasing testing time at 1200 °C as well, similar to the CS1. Since the differences between CS1 and CS2 are rather small on both alloys, further SEM micrographs are not displayed here. For CS2 on the 3-phase alloy the thickness of the IDZ is approximately 3 µm after 10 hours, 7.5 µm after 100 hours and 13.5 µm after 300 hours. The 2-phase alloy shows a larger IDZ with 4.5 µm after 10 h, 8 µm after 100 hours and 17 µm after 300 hours. Again, the 2-phase alloy shows a bigger IDZ after 300 hours than the 3-phase alloy.

4.Discussion

4.1. Coating system development with CTE adjustment

The first approach of this study contained a pure Si coating of about 15 µm on top of the 3-phase and the 2-phase alloy. On the one hand the coating develops successfully a SiO_2 TGO on the surface in order to potentially protect the alloy in Fig. 2 a) and b). On the other hand, the early failure of the coating becomes quite clear. The CTE mismatch between the Ti-containing Mo-Si based alloys and pure Si induced more cracks into the coatings that finally lead to failure. Once the oxygen met the substrate surface, Ti within the alloy reacted severely forming a fast growing TiO_2 which broke through the columnar gaps towards the surface. After deposition, the coating composed of columns with columnar gaps in between. The columnar gaps were only starting to close during the crystallization and the initial oxidation testing. Thus, a pathway for the oxygen was provided to potentially reach the substrate alloy itself before the cracks were filled with the oxides of Si and Ti. Moreover, TiO_2 has a significantly higher oxygen diffusion coefficient in the temperature range of 1200 °C (1.5 magnitude higher as SiO_2), thereby potentially channeling more oxygen into the substrate [22]. Consequently, a SiO_2 layer with embedded TiO_2 phase started to form along the interface between the Mo-Si-Ti based alloys and the Si-coating. This was followed by volume increase which created potentially tension, cracking and spallation. The SiO_2 oxidation layer with embedded TiO_2 was also found during oxidation tests of the uncoated Mo-Si-Ti alloys [9, 23].

After removing the coated sample from the furnace, probably the rapid cooling led to a severe spallation of the Si coating. Compared to the CTE of Mo-9Si-8B ($5 – 6 \times 10^{-6}$ °C^{-1} [24]) on which the Si coating was tested in previous studies, the Ti-macroalloyed substrates had a slightly higher CTE (Fig. 1) [18]. Titanium was thereby responsible for the higher CTE which was consistent to the study of Obert et al. where an alloy composition of Mo-20Si-52.8Ti (in at%) was investigated with a CTE of $7.0 – 9.1 \times 10^{-6}$ °C^{-1} (300 – 1200 °C) [25].

4.2. Influence of the PVD coating deposition parameters

Two coating systems were introduced in this study. The difference hereby lies within the deposition of the Si top layer. CS1 was produced in an industrial coater from interlayer to top layer identical to [19] (Fig. 3 a)). The top layer of CS2 was manufactured in a smaller sputter coater (Fig. 3 b) and c)). Two Si targets with a combined 0,75 kW target power were used with a target-substrate distance of 60 mm that is less than in CS1 which explains the 2 times higher deposition rate of the top layer in CS2 compared to CS1 described in the experimental part. The microstructure of CS1 showed a column width of about 2 – 2.8 µm, while in the structure of CS2 the Si top layer exhibited columns of a significantly greater width (3 – 4 µm) and larger inter-columnar gaps. The occurring broadening of the columnar structure can be explained by the rise in the homologous temperature $T_h > T_c$ where $T_c = 0.24$ stands for the critical homologous temperature. The homologous temperature with $T_h = 0.23$ is located in the structure zone model according to Thornton as well as according to Mukherjee and Gall in the zone T. Since the top layer of CS2 was deposited at a homologous temperature of $T_h = 0.23 < T_c$ ($T_h = T_s/T_m$ with $T_s = 383$ K) it resulted in an increase in the columnar broadening rate and thus a larger column width than for the top layer of CS1 ($T_h = 0.25 > T_c$ with $T_s = 422$ K) [26, 27]. The deviations in the microstructure can be further attributed to the target-substrate distance, which was reduced as a result of the change in the deposition system, as well as a changed rotation speed (IMPAX: 12 min^{-1}, Z400: 10 min^{-1}) and the differences in deposition rate.

As Messier [28] already showed, the bias voltage applied to the substrates has also an influence on the layer microstructure. In his adapted structure zone model, the bias voltage caused a zone T shift to lower temperatures, while the other zones remained unaffected. However, in a more advanced model, Anders [29] described that for Si, the bias stress also extended in zone 2 toward low temperatures. In agreement with this, Leisner [30] showed for Si coatings a narrowing as well as a significant increase in the number of columns after applying a substrate bias voltage of -100 V. This behavior can also be attributed to the Si top layer generated in this work. The Si top layer in CS2 was produced with a lower bias voltage of -10 V while CS1 was coated under a BIAS of -100 V. This suggests that in addition to the substrate temperature and the substrate rotation speed, the applied bias voltage had also a significant effect on the microstructure of Si coatings. Thus, an increasing bias voltage correlated with a decrease in column width as well as an increase in the column number. Furthermore, the application of a bias voltage to the substrates resulted in the implementation of Ar into the deposited Si coating. Accordingly, coatings prepared using a high bias voltage such as the Si top layers of CS1, showed an Ar concentration of 3 – 5 at% while in coatings applied at a low bias voltage of -10 V no clear Ar signal could be measured by EDS (Fig. 3 c)). The interlayers of CS1 and CS2 did not show a measurable Ar content as well. Though, the implementation of Ar could be prevented by an increased substrate temperature to 500 °C, although a bias of -50 V was applied in both systems for the interlayer. According to Mattox [31], a substrate temperature of 400 °C was sufficient for the gas atoms to desorb at the substrate surface before they are incorporated into the layer. The argon implementation in the Si layers had an effect on the porosity of the layers which is also discussed in [19]. The Si top layers of CS1 exhibited a (micro)porous structure in the oxidation tests already after 10 hours of oxidation, probably due to the evaporation of the remaining Ar in the coating during the exposure to 1200 °C, while the Si layers of CS2 had a dense structure even after 300 hours of oxidation. This suggests that the coating's porosity correlates with the Ar implementation in the coating, which in turn correlates

with the bias voltage applied to the substrates. Substrate temperature, geometrical factors of sample arrangements and sample rotation significantly influence the coating's growth and thus the microstructure. As a result of shadowing effects, the columnar growth direction as well as the column width and thus also the size of the columnar interstices were influenced. It was also found that a substrate bias voltage increases the density of amorphous coatings in the as-coated state, but a higher porosity develops once a subsequently high temperature exposure was performed. Using the same coating deposition parameters as in [19], the graded Mo-Si interlayer shows no significant change which proofs a great reproducibility by the PVD manufacturing process.

4.3. Isothermal oxidation behaviour of the Si-based dual layers on the Mo-Si-Ti alloys

The CS1 seemed to show a parabolic, diffusion-controlled growth rate of the SiO_2 TGO layers on the 3-phase as well as on the 2-phase alloy at 1200 °C in laboratory air up to 300 hours. The mass loss of the 2-phase alloy with CS1 was also reduced by the dual layer system, while the weight loss of the uncoated 3-phase alloy was almost completely suppressed due to protective coatings, resulting in a mass increase of only 0.02 % after 300 hours. Layer spallation was identified on the 2-phase alloy. PVD processes are known to create homogenous all-around coatings on the substrate material. Due to the limitation of the samples the reason of spallation, especially the location, cannot be identified in detail. The edges are usually more affected by spalling due to stresses which was not observed in Fig. 5 on the 2-phase alloy. A possible explanation could be the usage of substrate bias voltage that normally effects edges more, but this would need more statistical research by providing more samples in future studies. Another reason could be sporadic micropores in the alloys (not shown in the paper) during manufacturing which lead to the spallation. Furthermore, exposures to the pest critical temperature of 800 °C showed the complete suppression of pest corrosion for a period of 100 hours for the two alloys. After testing at 800 °C, no oxide phases were detected above the interlayers despite an oxygen concentration of approx. 35 at% (Fig. 9). Within the interlayer,

the oxygen most likely forms Si oxides due to the lower Gibbs energy of SiO_2 compared to Mo-oxides but a detailed measurement by TEM is still pending to prove this [16, 32]. Both CS1 and CS2 provided perfect protection against pest oxidation for both alloys.

CS2 also formed at higher temperatures protective TGO layers with almost the same thickness than for CS1. But the samples of CS2 indicated significantly higher mass changes than those of CS1 (Fig. 4). The XRD did not show any significant difference compared to CS1 in Fig. 10. SiO_2 implemented in the Si layer was also formed in CS2, above the Mo-Si interlayer. Already after 100 hours, spallation appeared on the 2-phase alloy, whereas the layers on the 3-phase alloy remained almost intact. Up to 100 hours at 1200 °C, the 2-phase and 3-phase samples showed only marginal mass changes. For longer oxidations, however, layer spalling (2-phase) and oxidation-induced mass increases (3-phase) became apparent (Fig. 6). Compared to CS1, the weight reduction of the 2-phase alloy also increased which can be attributed to the extensive layer spalling. The mass increase of the 3-phase alloy due to oxidation products was higher compared to CS1 which can be attributed to oxide formation.

According to the assessment of Deal and Grove, SiO_2 is formed predominantly by inward diffusion of oxygen [33]. The only SiO_2 allotrope detected in the TGO layers was α-cristobalite (Fig. 12 a) and b)). Due to layer spallation, the determination of the mass change did not allow any conclusion on the oxidation kinetics of the TGO layers. However, observation of the SiO_2 TGO layer thicknesses plotted against the oxidation shows a parabolic growth curve (Fig. 7). Investigations showed that a correlation can be established between the film thickness profile and the mass change relative to the surface [34]. Accordingly, a parabolic diffusion-controlled oxidation mechanism can be assumed for the development of the SiO_2 TGO layers that is consistent with mostly oxygen inward diffusion.

Segmentation cracks were detected in the TGO in isolated cases after 300 hours of oxidation. These was attributed to thermally induced biaxial stresses due to the different coefficients of

thermal expansion of Si (2.6×10^{-6} °C^{-1}, 25 °C) and the polymorphic SiO_2. During the cooling process at about 220 °C, cristobalite transforms from the β-phase (3.1×10^{-6} °C^{-1}) to the α-phase (10.3×10^{-6} °C^{-1}) accompanied by a specific volume reduction of 2.8 – 4.5 % [35, 36]. The induced stresses can lead to crack initiation and propagation within the TGO SiO_2 layers. The dual layer coated 2-phase alloy showed the formation of a pure SiO_2 TGO on both coating systems (Fig. 11 and Fig. 17). On the coated 3-phase alloy, Fe oxide particles were detected in the TGO layers already after 100 hours of testing at 1200 °C in both coating systems (Fig. 10 and Fig. 16). The XRD results (Fig. 12 a)) identify them as Fe_2O_3 which explains the brownish coloured surface of the coated 3-phase alloys (see macroscopic picture in Fig. 5 and Fig. 6) [37]. The formation of the Fe oxide precipitates suggests that Fe diffused from the 3-phase substrate alloy through the Mo-Si interlayer and the Si top layer into the TGO of SiO_2, where it precipitated as Fe oxide (Fe_2O_3) due to the reaction with the inward diffused oxygen (Fig. 10 d) and Fig. 16 d)). Ramappa and Henly investigated the diffusion of Fe in SiO_2 and found that Fe preferentially segregates in SiO_2 at the interface to Si [38]. The Si/SiO_2 interface was described as a sink of impurities. Moreover, it was suggested that Fe tend to accumulate in the Si oxide near the interface and that this was described as a pileup characteristic which provided a discontinuity in the concentration profile of Fe from the oxide into Si [38-41]. Kamiura et al. observed further that if Fe was dissolved in Si, the most of the Fe atoms accumulated at the Si/SiO2 interface [41]. For the present coating it was likely that the 2 at% of Fe diffused through the dual layer coating system in the early stages of oxidation testing (< 100 hours). The TGO thickness was approximately less than 1.5 µm when Fe piled up at the Si/SiO_2 interface (Fig. 7). Due to the oxygen inward diffusion the Fe oxidized and segregated slowly into visible precipitates after 300 hours. Simultaneously to this the Si/SiO_2 interface travelled further into the Si top layer leaving the Fe oxide precipitates in the upper third of the TGO. The current finding can be also interpreted in terms of ion flux. Since the Fe_2O_3 precipitates were approximately in the middle of the TGO, this also means that the cation and

anion flux were relatively balanced in the SiO_2 TGO. If the cation flux was higher, the metals would diffuse comparatively faster, and the Fe_2O_3 would have to be on the surface, if the anion flux was higher, the Fe_2O_3 particles would have to precipitate at the Si/SiO_2 interface. Both unbalanced cases did not occur [42, 43].

The oxidation behaviour of the pure alloys presented an advanced degraded 3-phase alloy with a SiO_2/TiO_2 duplex oxide scale and internal oxidation, see Fig. 8 a), which corresponded greatly with the mass changes in Fig. 4. The oxide scale of the 2-phase alloy in Fig. 8 b) was about 100 µm thick accompanied with an internal oxidation of about 100 µm. The vaporisation of MoO_3 and the oxide formation seemed to balance each other out no relevant mass change could be detected in Fig. 4. Furthermore the oxidation behaviour of the alloys was intensively studied in [6] and [9]. The 3-phase alloy showed an oxidation layer of about 50 µm after 100 hours of isothermal testing at 1100 °C [6], the 2-phase alloy was analysed after 100 hours of isothermal testing at 1200 °C with a oxidation layer of about 68 µm [9]. Schliephake et al. [15] enhanced the oxidation resistance of an Mo-Si-Ti alloy, which corresponds to the composition of the 3-phase alloy except for 2 at% Fe content, via pack cementation. For this purpose, Si and B were deposited by co-pack cementation and formed a approx. 150 µm thick system of borosilicate with embedded TiO_2, $MoSi_2$, Ti_5Si_3. The isothermal oxidation tests of 100 hours yielded a mass decrease of maximum 4 mg/cm^2 at 800 °C. At 1200 °C the weight change was negligible which was attributed to the $MoSi_2$ layer that acted as a diffusion barrier for Ti due to negligible solubility of Ti in $MoSi_2$. In this work, the CS1 on the 3-phase alloy showed an even better oxidation resistance with a mass decrease of 0.3 mg/cm^2 after 100 hours at 800 °C and 0.1 mg/cm^2 after 300 hours at 1200 °C, respectively. In summary, both CS1 and CS2 protected the alloys for oxidation at 800 °C and 1200 °C compared to the pure alloy performance. Due to heavy spallation of CS2, CS1 showed a better overall performance. Compared to the results in [19] where CS1 was coated on a Mo-9Si-8B alloy the TGO followed the same parabolic growth rate. The interface between interlayer and top layer was highly influenced by the SiO_2

and TiO_2 built-up on the Mo-Si-Ti-B-(Fe) alloys presented in this study while in [19] the Mo-9Si-8B alloys had only minor SiO_2 formation within the interlayer.

4.4. Interdiffusion processes between the 3-phase and 2-phase substrate alloy and the dual layer coating systems

After oxidation tests at 800 °C for 100 hours oxidation, no formation of an interdiffusion zones was observed. The XRD scans in Fig. 12 a) and b) of the as-coated systems confirm crystallized phases of Mo_5Si_3 and $MoSi_2$ before the initial annealing. The oxygen within the interlayer after deposition (Fig. 3 c)) and the oxygen inwards diffusion after testing for 10 hours at 1200 °C led to SiO_2 formation at the columnar gaps in the Mo-Si interlayers as well as in the Si top layers. The SiO_2 with embedded TiO_2 particles formed an almost continuous region between inter- and top layer. The appearance of SiO_2 can be explained by the lower Gibbs energy of SiO_2 compared to the phases Mo_5Si_3 and $MoSi_2$ [32, 44]. SiO_2 can act as a barrier for further oxygen inward diffusion [18]. The formation of a SiO_2 layer at a Mo-Si interface prevents the formation of Mo-silicide as it was similarly shown by Rastogi et al [20]. These results are consistent with the XRD scans in this work. With increasing testing time, a reduction of mostly the $MoSi_2$ phase can be found (Fig. 12). Thus, successive dissolution of this phase probably occurs at a temperature of 1200 °C. The disappearance of the $MoSi_2$ phase in coating systems was also found in [45, 46] which agrees with the XRD data in this work. Already after 10 hours, hardly any $MoSi_2$ was detected (Fig. 12).

Above the interlayer in CS1 and 2, an increased pore formation occurs in the Si top layer after an oxidation of 300 hours (Fig. 10 c), Fig. 11 c), Fig. 16 c), Fig. 17 c)) triggered by the inward diffusion of the Si to the Mo-Si interlayer. Since Si has a high diffusion rate in Mo, it diffuses towards the substrate alloys despite the Si oxide formation which leads to Kirkendall pores [47, 48]. In the remaining area of the Si top layer of CS1, uniformly distributed porosities can also be seen after 10 hours, which agglomerate with increasing oxidation. In addition to the Kirkendall effect, this porosity in CS1 was presumably also a result from implementation of

argon into the layer due to the applied higher bias voltage during the magnetron sputter process as described above.

For the dual coating systems on the 3-phase and 2-phase alloy, the formation of Ti oxides in addition to SiO_2 can be detected in the Mo-Si interlayer after 100 hours at 1200 °C. This formation of rutile (identified by XRD, Fig. 12, and electron diffraction using TEM, Fig. 14) occurred mainly at the interface between interlayer and top layer. This suggested that Ti diffused from the substrate alloy through the Mo-Si interlayer in the direction of the incorporated oxygen due to the high oxygen affinity. In this area, severe spallation occurred probably during the cooling process, especially on the 2-phase alloy (Fig. 5 and Fig. 6). The diverging CTEs of Si and SiO_2 as well as the transformation of β- to α-cristobalite and the associated changes in volume led to significant stresses within the layered composites. In addition, Ti-oxide has also a significantly higher CTE (e.g. TiO_2: 8.4×10^{-6} °C^{-1} [49]) than Si and thus contributed decisively to the formation of thermally induced stresses and therefore spallation between interlayer and top layer. Since the majority of the spalling occurred on the 2-phase alloy, it can be assumed that the Ti content of 34 at%, compared to the 3-phase alloy with only 27.5 at% Ti, led to an increased formation of Ti oxides.

The differently manufactured top layers CS1 and CS2 had no influence on the interlayer-substrate surface performance, but the composition of the base alloy had a significant effect. In the substrate surfaces of the 3-phase as well as the 2-phase alloy an interdiffusion zone (IDZ) was formed (Fig. 14 and Fig. 15 respectively) as already found on a Mo-9Si-8B alloy in previous work [19]. The adhesion of the dual layer coating system was probably enhanced due to the development of such IDZ, which increased in width with testing time (Fig. 13). The present work shows that the extent of IDZ formation is substrate-specific while the influence of the individual silicon coating system on top was negligible. Si is more mobile with respect to the diffusion in the Mo-Si phases due to the higher defect concentration within the Si

sublattice and the smaller atomic size compared to Mo [50]. Accordingly, Si diffused from the coating system into the Mo-rich alloys and an IDZ of an Si-enriched alloy was formed during the oxidation tests at 1200 °C. The formed IDZ became more homogeneous with increasing testing time (Fig. 13) by changing the microstructure of the alloy and transforming the original phases. After 300 hours, the IDZ consisted to a great part of $(Mo,Ti)_5Si_3$. In the alloys $(Ti,Mo)_5Si_3$, Ti_5Si_3 and some internal oxidation of TiO_2 and SiO_2 can be found which is underlined by the TEM observations in Fig. 14 and Fig. 15. This was in good agreement with the pack cementation coating on the 3-phase alloy in [15] where the layer closest to the substrate consisted of Ti_5Si_3 with $MoSi_2$ and Mo_5Si_3 particles embedded. Irrespective of this, oxygen also diffused into the substrate alloy, which after 300 hours led locally to the formation of 2 µm large island-shaped Ti oxide phases within the IDZ. This was accompanied by the formation of pores, which were localised in the direct vicinity of the Ti oxide phases.

The 2-phase alloy consisted of both the Mo_{ss}/Ti_{ss} phase and the mixed phase $(Mo,Ti)_5Si_3$. Since Ti has an almost unlimited solubility in Mo, the Mo_{ss} has up to 25 at% and the $(Mo,Ti)_5Si_3$ phase up to 45 at% Ti in the initial state [51]. The resulting concentration indicated the transformation of the solid solution into the $(Mo,Ti)_5Si_3$ phase. As a result, the phases visible in the interdiffusion zone differed only in their Ti content between 13 and 25 at%, suggesting that a rather homogeneous IDZ was formed with increasing diffusion time. In the TEM analyses (Fig. 15) the Ti_5Si_3 phase could also be identified but could not be analysed by SEM measurements due to its rare presence within the IDZ.

Independently of the respective alloys, pores were detected at the interlayer-substrate interface after almost all testing states at 1200 °C, which formed a line in this area (Fig. 10, Fig. 11, Fig. 16, Fig. 17). In most cases, the pores in this area were filled with SiO_2, which formed in the free spaces due to Si outwards and oxygen inwards diffusion. As in [19], an increase in the oxidation time at 1200 °C also led to a spreading of the IDZ in this work to about 7 µm. This

suggested that the growth of the IDZ correlates with both temperature and oxidation time. The difference in thickness of the IDZ between the individual coating systems CS1 and CS2 was only minimal, so as expectable no influence of the deposition process of the Si top layer was noticed. However, differences between the alloys could be seen. The growth of the IDZ thicknesses followed in all cases an approximately linearly increasing trend over the oxidation time. The IDZ of the 3-phase and 2-phase alloys were 2 and 2.5 times thicker, respectively, in comparison to the IDZ formed on the Mo-9Si-8B alloy [19]. This suggested that the diffusion of the Ti into the layer simultaneously led to an enhanced diffusion of Si into the substrate. Although the 2-phase alloy had a higher Si content but lower Mo content (21 at% Si, 44.5 at% Mo) compared to the 3-phase alloy (12.5 at% Si, 49.5 at% Mo), the IDZ of the 2-phase alloy was bigger. The different microstructures of the alloys and the constituting phases are possible explanations. The 2-phase alloy has a fine lamellar microstructure with a high density of grain boundaries whereas the 3-phase alloy consists of larger grains (Fig. 1). Moreover, the 3-phase alloy contains the Mo_5SiB_2 phase which is known as diffusion barrier of Si [52]. Overall, the 2-phase alloy seemed to have an increasing effect on Si diffusion with a 27 % larger IDZ than the 3-phase alloy and a 100 % larger IDZ than the Mo9Si8B alloy.

5. Conclusions

The alloys Mo-12.5Si-8.5B-27.5Ti-2Fe and Mo-21Si-34Ti-0.5B (at%) were coated with two different coating systems by magnetron sputtering to provide a sufficient oxidation protection at temperatures up to 1200 °C until 300 hours. Two coating systems were developed consisting of a Mo-Si graded interlayer and a Si top layer. The interlayer provided enhanced adhesion with the Si top layer because a pure Si coating could not protect the alloys due to cracks that were induced by massive TiO_2 growth. In coating system 1 the applied bias voltage led to Ar implementation and pore formation after testing at 1200 °C. Coating system 2 had a different morphology of the Si top layer with larger columns and columnar gaps. Both coating systems developed a protective SiO_2 thermally grown oxide layer on top of the Si coating with a

parabolic growth rate. At the interface between top layer and interlayer, SiO_2 with embedded TiO_2 particles formed with increasing oxidation time, building a weak spot for coating spallation which could be observed especially on the Mo-21Si-34Ti-0.5B alloy. Nevertheless, Ti could be hindered to diffuse into the Si top layer by applying the Mo-Si interlayer. This was a clear improvement over the single layer Si coating. An interdiffusion zone (IDZ) between interlayer and alloy grew with increasing testing time that contains mostly $(Mo,Ti)_5Si_3$. Presumably due to its microstructure and higher Ti content, the Mo-21Si-34Ti-0.5B alloy showed a 27 % bigger IDZ compared to the Mo-12.5Si-8.5B-27.5Ti-2Fe alloy. The 2 at% Fe within the Mo-12.5Si-8.5B-27.5Ti-2Fe alloy where able to diffuse into the TGO forming Fe_2O_3 particles.

Both coatings fully protected the underlying alloys against pest oxidation at 800°C. The oxidation protection at 1200 °C in terms of TGO thicknesses, spallation and weight change favoured the coating system 1 over the coating system 2 and the Mo-12.5Si-8.5B-27.5Ti-2Fe over the Mo-21Si-34Ti-0.5B. Nevertheless, compared to the uncoated alloys both magnetron sputtered coating systems can protect the alloys by suppressing severe oxidation processes at 800 °C and 1200 °C isothermally tested which has been shown here for the first time for these new alloys.

6.Data availability statement

The raw and processed data required to reproduce these findings are available on request to ronja.anton@dlr.de.

7.Acknowledgment

This study was conducted under the financial support of Deutsche Forschungsgemeinschaft (DFG) within the framework of grants no. SCHU 1372/7-2, GO 2283/3-2 and HE1872/33-1 which is gratefully acknowledged. The authors thank their project partners S. Obert, Dr.-Ing. A. Kauffmann who produced the substrate material and provided scientific support. Part of this work was performed at the Micro- and Nanoanalytics Facility (MnaF) of the University of Siegen. Thanks to Dr.-Ing. J. Müller from the University of Siegen for the TEM support. We

thank Dr. P. Mechnich for the CTE measurements and analyses. For the scientific and technical support at the German Aerospace Centre, the authors thank V. Leisner, P.-P. Bauer, and J. Brien. For lamella preparation with FIB, we like to thank F. Kreps and for further TEM support we thank K. Kelm.

8. References

[1] H. J. Grabke and G. H. Meier, Accelerated Oxidation, Internal Oxidation, Intergranular Oxidation, and Pesting of Intermetallic Compounds, Oxidation of Metals 44. 1-2 (1995) 147-176. 10.1007/Bf01046726

[2] I. Rosales, H. Martinez, D. Bahena, J. A. Ruiz, R. Guardian, and J. Colin, Oxidation performance of Mo3Si with Al additions, Corrosion Science 51. 3 (2009) 534-538. 10.1016/j.corsci.2008.12.004

[3] D. A. Berztiss, R. R. Cerchiara, E. A. Gulbransen, F. S. Pettit, and G. H. Meier, Oxidation of Mosi2 and Comparison with Other Silicide Materials, Materials Science and Engineering a-Structural Materials Properties Microstructure and Processing 155. 1-2 (1992) 165-181. Doi 10.1016/0921-5093(92)90324-T

[4] R. W. Bartlett, J. W. McCAMONT, and P. R. GAGE, Structure and Chemistry of Oxide Films Thermally Grown on Molybdenum Silicides, 48. 11 (1965) 551-558. https://doi.org/10.1111/j.1151-2916.1965.tb14671.x

[5] K. Natesan and S. C. Deevi, Oxidation behavior of molybdenum silicides and their composites, Intermetallics 8. 9-11 (2000) 1147-1158. Doi 10.1016/S0966-9795(00)00060-1

[6] M. A. Azim, D. Schliephake, C. Hochmuth, B. Gorr, H. J. Christ, U. Glatzel, and M. Heilmaier, Creep Resistance and Oxidation Behavior of Novel Mo-Si-B-Ti Alloys, Jom 67. 11 (2015) 2621-2628. 10.1007/s11837-015-1560-z

[7] Y. Yang, Y. A. Chang, L. Tan, and W. Cao, Multiphase equilibria in the metal-rich region of the Mo–Ti–Si–B system: thermodynamic prediction and experimental validation, Acta Materialia 53. 6 (2005) 1711-1720. 10.1016/j.actamat.2004.12.020

[8] D. Schliephake, M. Azim, K. von Klinski-Wetzel, B. Gorr, H.-J. Christ, H. Bei, E. P. George, and M. Heilmaier, High-Temperature Creep and Oxidation Behavior of Mo-Si-B Alloys with High Ti Contents, Metallurgical and Materials Transactions A 45. 3 (2014) 1102-1111. 10.1007/s11661-013-1944-z

[9] D. Schliephake, A. Kauffmann, X. Cong, C. Gombola, M. Azim, B. Gorr, H.-J. Christ, and M. Heilmaier, Constitution, oxidation and creep of eutectic and eutectoid Mo-Si-Ti alloys, Intermetallics 104. (2019) 133-142. 10.1016/j.intermet.2018.10.028

[10] C. Gatzen, I. Smokovych, M. Scheffler, and M. Krüger, Oxidation-Resistant Environmental Barrier Coatings for Mo-Based Alloys: A Review, Advanced Engineering Materials 23. 4 (2021) 2001016. https://doi.org/10.1002/adem.202001016

[11] J. H. Perepezko and C. Harris, Oxidation of Mo-Si-B Alloys and Coatings in a Water Vapor Environment, Oxidation of Metals 96. 3 (2021) 323-332. 10.1007/s11085-021-10064-5

[12] A. Lange and R. Braun, Magnetron Sputtered Oxidation Protection Coatings for Mo-Si-B alloys, Corrosion Science 84. (2014) 74-84.

[13] I. Smokovych, G. Hasemann, M. Krüger, and M. Scheffler, Polymer derived oxidation barrier coatings for Mo-Si-B alloys, Journal of the European Ceramic Society 37. 15 (2017) 4559-4565. 10.1016/j.jeurceramsoc.2017.06.048

[14] J. Yang, H. Liu, W. Gao, L. Su, and K. Jiang, Effect of different fillers on the microstructural evolution and high temperature oxidation resistance of Mo-Si-B coatings prepared by pack cementation, International Journal of Refractory Metals and Hard Materials 100. (2021) 105625. https://doi.org/10.1016/j.ijrmhm.2021.105625

[15] D. Schliephake, C. Gombola, A. Kauffmann, M. Heilmaier, and J. H. Perepezko, Enhanced Oxidation Resistance of Mo–Si–B–Ti Alloys by Pack Cementation, Oxidation of Metals 88. 3-4 (2017) 267-277. 10.1007/s11085-017-9730-8

[16] S. Majumdar, B. Paul, P. K. Singh, J. Kishor, and V. Kain, Effect of Si content on microstructure, mechanical and oxidation properties of hot pressed Mo-Ti-Si alloys, Intermetallics 100. (2018) 126-135. https://doi.org/10.1016/j.intermet.2018.06.013

[17] S. Majumdar, Isothermal and cyclic oxidation resistance of pack siliconized Mo–Si–B alloy, Applied Surface Science 414. (2017) 18-24. https://doi.org/10.1016/j.apsusc.2017.03.300
[18] R. Anton, N. Laska, U. Schulz, S. Obert, and M. Heilmaier, Magnetron Sputtered Silicon Coatings as Oxidation Protection for Mo-Based Alloys, Advanced Engineering Materials 22. 7 (2020) 2000218. 10.1002/adem.202000218
[19] R. Anton, S. Hüning, N. Laska, M. Weber, S. Schellert, B. Gorr, H.-J. Christ, and U. Schulz, Graded PVD Mo-Si interlayer between Si coating and Mo-Si-B alloys: Investigation of oxidation behaviour, Corrosion Science 192. (2021) 109843. https://doi.org/10.1016/j.corsci.2021.109843
[20] R. S. Rastogi, V. D. Vankar, and K. L. Chopra, The Effect of Oxygen Impurity on Growth of Molybdenum Disilicide and Its Distribution during Rapid Thermal Annealing of Co-Sputtered Mosix Thin-Films, Thin Solid Films 213. 1 (1992) 45-54. Doi 10.1016/0040-6090(92)90473-O
[21] T. Mizushima, Y. Moriya, N. H. H. Phuc, H. Ohkita, and N. Kakuta, Soft chemical transformation of α-MoO3 to β-MoO3 as a catalyst for vapor-phase oxidation of methanol, Catalysis Communications 13. 1 (2011) 10-13. https://doi.org/10.1016/j.catcom.2011.06.012
[22] W. D. Kingery, H. K. Bowen, and D. R. Uhlmann, Introduction to ceramics. John wiley & sons, 1976 0471478601.
[23] S. Majumdar, P. K. Singh, A. K. Pandey, and G. V. S. N. Rao, Kinetics of oxide scale growth on a (Ti, Mo)5Si3 based oxidation resistant Mo-Ti-Si alloy at 900-1300∘C %J High Temperature Materials and Processes, 38. 2019 (2019) 533-540. doi:10.1515/htmp-2019-0056
[24] A. Lange, M. Heilmaier, T. A. Sossamann, and J. H. Perepezko, Oxidation behavior of pack-cemented Si–B oxidation protection coatings for Mo–Si–B alloys at 1300°C, Surface and Coatings Technology 266. (2015) 57-63. https://doi.org/10.1016/j.surfcoat.2015.02.015
[25] S. Obert, A. Kauffmann, S. Seils, T. Boll, S. Kauffmann-Weiss, H. Chen, R. Anton, and M. Heilmaier, Microstructural and chemical constitution of the oxide scale formed on a pesting-resistant Mo-Si-Ti alloy, Corrosion Science 178. (2021) 109081. https://doi.org/10.1016/j.corsci.2020.109081
[26] S. Mukherjee and D. Gall, Structure zone model for extreme shadowing conditions, Thin Solid Films 527. (2013) 158-163. https://doi.org/10.1016/j.tsf.2012.11.007
[27] O. Madelung, U. Rössler, and M. Schulz, Silicon (Si), Debye temperature, heat capacity, density, hardness, melting point, Landolt-Börnstein Substance/Property Index 41. (2002) 1-16.
[28] R. Messier, A. P. Giri, and R. A. Roy, Revised Structure Zone Model for Thin-Film Physical Structure, Journal of Vacuum Science & Technology a-Vacuum Surfaces and Films 2. 2 (1984) 500-503. Doi 10.1116/1.572604
[29] A. Anders, A structure zone diagram including plasma-based deposition and ion etching, Thin Solid Films 518. 15 (2010) 4087-4090. https://doi.org/10.1016/j.tsf.2009.10.145
[30] V. Leisner, "Neue Environmental Barrier Coatings für SiC/SiC-Faserverbundwerkstoffe durch PVD-Technologien," Ph.D. thesis, Karlsruher Institut für Technologie (KIT), 2020.
[31] D. M. Mattox, Handbook of Physical Vapor Deposition (PVD) Processing (Handbook of Physical Vapor Deposition (PVD) Processing). 2010
[32] A. Heintz, "Thermodynamik der Mischungen und Mischphasengleichgewichte," in Thermodynamik der Mischungen: Mischphasen, Grenzflächen, Reaktionen, Elektrochemie, äußere KraftfelderBerlin, Heidelberg Springer Berlin Heidelberg, 2017, pp. 1-195. 10.1007/978-3-662-49924-5_1 978-3-662-49924-5.

[33] B. E. Deal and A. S. Grove, General Relationship for the Thermal Oxidation of Silicon, Journal of Applied Physics 36. 12 (1965) 3770-3778. 10.1063/1.1713945
[34] R. Anton, V. Leisner, P. Watermeyer, M. Engstler, and U. Schulz, Hafnia-doped silicon bond coats manufactured by PVD for SiC/SiC CMCs, Acta Materialia 183. (2020) 471-483. 10.1016/j.actamat.2019.10.050
[35] J. Rodríguez-Viejo, F. Sibieude, M. Clavaguera-Mora, and C. Monty, O diffusion through amorphous SiO2 and cristobalite, Applied physics letters 63. 14 (1993) 1906-1908.
[36] B. T. Richards, S. Sehr, F. de Franqueville, M. R. Begley, and H. N. G. Wadley, Fracture mechanisms of ytterbium monosilicate environmental barrier coatings during cyclic thermal exposure, Acta Materialia 103. (2016) 448-460. 10.1016/j.actamat.2015.10.019
[37] "Colour Plates," in The Iron Oxides, 2003, pp. xxi-xxxix. https://doi.org/10.1002/3527602097.ins
[38] D. A. Ramappa and W. B. Henley, Diffusion of Iron in Silicon Dioxide, Journal of The Electrochemical Society 146. 10 (1999) 3773-3777. 10.1149/1.1392548
[39] B. E. Deal and C. R. Helms, The physics and chemistry of SiO2 and the Si-SiO2 interface. Springer Science & Business Media, 2013 1489907742.
[40] A. Ohsawa, K. Honda, and N. J. J. o. t. E. S. Toyokura, Metal Impurities near the SiO2-Si Interface, 131. 12 (1984) 2964.
[41] Y. Kamiura, F. Hashimoto, and M. Iwami, Observation of iron pileup and reduction of SiO2 at the Si-SiO2 interface, 53. 18 (1988) 1711-1713. 10.1063/1.99802
[42] M. P. Brady, I. G. Wright, and B. Gleeson, Alloy design strategies for promoting protective oxide-scale formation, JOM 52. 1 (2000) 16-21. 10.1007/s11837-000-0109-x
[43] D. R. Clarke, The lateral growth strain accompanying the formation of a thermally grown oxide, Acta Materialia 51. 5 (2003) 1393-1407. https://doi.org/10.1016/S1359-6454(02)00532-3
[44] H. Fujiwara and Y. Ueda, Thermodynamic properties of molybdenum silicides by molten electrolyte EMF measurements, Journal of Alloys and Compounds 441. 1-2 (2007) 168-173. 10.1016/j.jallcom.2006.07.128
[45] R. Sakidja, J. S. Park, J. Hamann, and J. H. Perepezko, Synthesis of oxidation resistant silicide coatings on Mo–Si–B alloys, Scripta Materialia 53. 6 (2005) 723-728. https://doi.org/10.1016/j.scriptamat.2005.05.015
[46] Z. Tang, A. J. Thom, M. J. Kramer, and M. Akinc, Characterization and oxidation behavior of silicide coating on multiphase Mo–Si–B alloy, Intermetallics 16. 9 (2008) 1125-1133. https://doi.org/10.1016/j.intermet.2008.06.014
[47] A. Paul, "Diffusion Rates of Components in Metal-Silicides Depending on Atomic Number of Refractory Metal Component," in Diffusion Foundations, 2019, vol. 21, pp. 29-84: Trans Tech Publ.
[48] J.-K. Yoon, G.-H. Kim, J.-Y. Byun, J.-S. Kim, and C.-S. Choi, Simultaneous growth mechanism of intermediate silicides in MoSi2/Mo system, Surface and Coatings Technology 148. 2 (2001) 129-135. https://doi.org/10.1016/S0257-8972(01)01354-8
[49] E. Meagher and G. A. Lager, Polyhedral thermal expansion in the TiO 2 polymorphs; refinement of the crystal structures of rutile and brookite at high temperature, The Canadian Mineralogist 17. 1 (1979) 77-85.
[50] S. Prasad and A. Paul, Growth mechanism of phases by interdiffusion and atomic mechanism of diffusion in the molybdenum–silicon system, Intermetallics 19. 8 (2011) 1191-1200. https://doi.org/10.1016/j.intermet.2011.03.027

[51] Y. Yang, H. Bei, S. Chen, E. P. George, J. Tiley, and Y. A. Chang, Effects of Ti, Zr, and Hf on the phase stability of Mo_ss+Mo3Si+Mo5SiB2 alloys at 1600°C, Acta Materialia 58. 2 (2010) 541-548. 10.1016/j.actamat.2009.09.032

[52] S. Kim and J. H. Perepezko, Interdiffusion kinetics in the Mo5SiB2 (T2) phase, Journal of Phase Equilibria and Diffusion 27. 6 (2006) 605-613. 10.1007/BF02736562

List of figure captions

Figure 1 a) CTE versus temperature of the 3-phase and 2-phase alloy; secondary electron SEM cross-sectional micrographs of the microstructure of the manufactured 3-phase alloy b); the 2-phase alloy c).

Figure 2 Secondary electron SEM cross-sectional micrographs of a pure Si coating a) deposited on the 3-phase alloy with a close up of the TGO and b) deposited on the 2-phase alloy with a close up of the TGO; both after 100 hours of isothermal exposure at 1200 °C in laboratory air.

Figure 3 Secondary electron SEM micrographs of the cross section of the dual coating system after deposition by magnetron sputtering, a) CS1 b) CS2 c) CS2 with EDS line scan in at%, deposited on a TZM substrate.

Figure 4 Mass change versus time during isothermal testing at 1200 °C until 300 hours of 3-phase alloy and 2-phase alloy (uncoated, with CS1 and with CS2).

Figure 5 CS1 macro images of the at 1200 °C isothermal tested uncoated and coated 3-phase alloy as well as the uncoated and coated 2-phase alloy.

Figure 6 CS2 macro images of the isothermal tested coated 3-phase alloy and coated 2-phase alloy.

Figure 7 SiO_2 TGO growth depending on the isothermal exposure time of the CS1 and CS2 deposited on the 3-phase and 2-phase alloy with a parabolic trendline at 1200°C in laboratory air.

Figure 8 Secondary electron SEM cross-sectional micrograph a) of the uncoated 3-phase alloy; b) of the uncoated 2-phase alloy after 300 hours at 1200 °C.

Figure 9 a) Mass change versus time during isothermal testing at 800 °C until 100 hours of 3-phase alloy and 2-phase alloy uncoated, with CS1 and with CS2; b) Macro images of the 3-phase and 2-phase alloy isothermal tested at 800 °C for 100 hours uncoated, with CS1 and with CS2.

Figure 10 Secondary electron SEM cross-sectional micrographs of the CS1 deposited on 3-phase alloy, after a) 10 hours, b) 100 hours with a close up of the interface and c) 300 hours, d) close up of TGO; e) EDS mapping of TGO in at% after 300 hours of isothermal exposure to 1200 °C in laboratory air.

Figure 11 Secondary electron SEM cross-sectional micrographs of the CS1 deposited on 2-phase alloy, after a) 10 hours, b) 100 hours with a close up of the interface and c) 300 hours of isothermal exposure to 1200 °C in laboratory air.

Figure 12 XRD scans of the CS1, deposited on a) 3-phase alloy in as-coated state, after 10, 100 and 300 hours, and deposited on b) 2-phase alloy in as-coated state, after 10, 100 and 300 hours isothermal exposure time at 1200 °C in laboratory air.

Figure 13 Secondary electron SEM cross-sectional micrographs showing the CS1 evolution of the interdiffusion zone, deposited on 3-phase alloy, after a) 10, b) 100 and c) 300 hours, and

deposited on 2-phase alloy, after d) 10, e) 100 and f) 300 hours isothermal exposure time at 1200 °C in laboratory air. For better visibility, the IDZ is marked by a light red colour band.

Figure 14 TEM analyses of the coated 3-phase alloy after 300 hours of oxidation at 1200 °C; a) HAADF STEM of the 3-phase IDZ and Mo-Si interlayer; b) – e) EDS element mappings showing the Mo, Si, Ti and O parts in at%; f) SAED pattern and crystal plane of the in a) marked grains.

Figure 15 TEM analyses of the coated 2-phase alloy after 300 hours of oxidation at 1200 °C; a) HAADF STEM of the 2-phase IDZ and Mo-Si interlayer; b) – e) EDS element mappings showing the Mo, Si, Ti and O parts in at%; f) SAED pattern and crystal planes of the in a) marked grains.

Figure 16 Secondary electron SEM cross-sectional micrographs of the CS2 deposited on 3-phase alloy, after a) 10, b) 100 and c) 300 hours; d) close up of TGO; e) EDS mapping of TGO in at% after 300 hours of isothermal exposure at 1200 °C in laboratory air.

Figure 17 Secondary electron SEM cross-sectional micrographs of the CS2 deposited on 2-phase alloy, after a) 10, b) 100 and c) 300 hours of isothermal exposure at 1200 °C in laboratory air.

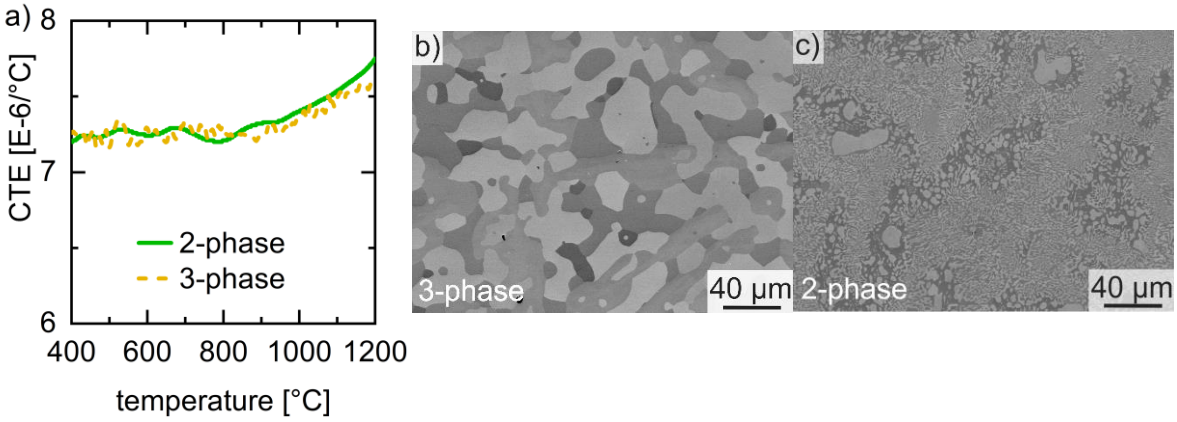

Figure 1

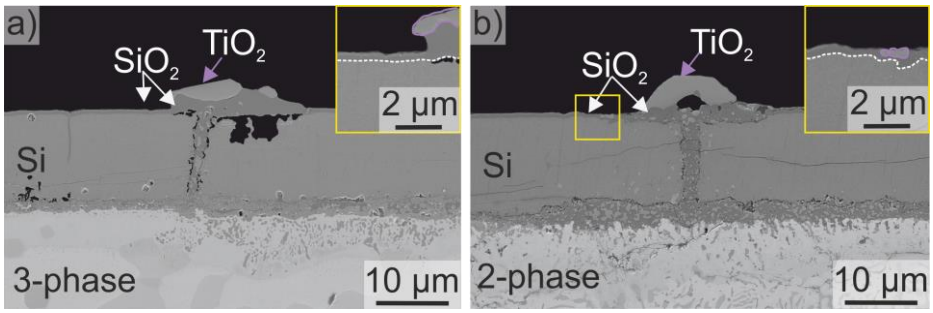

Figure 2

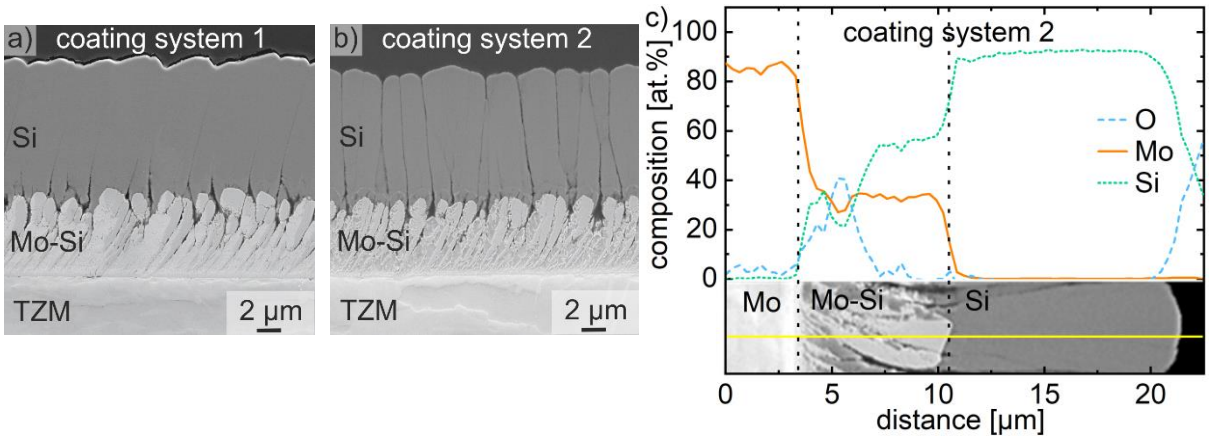

Figure 3

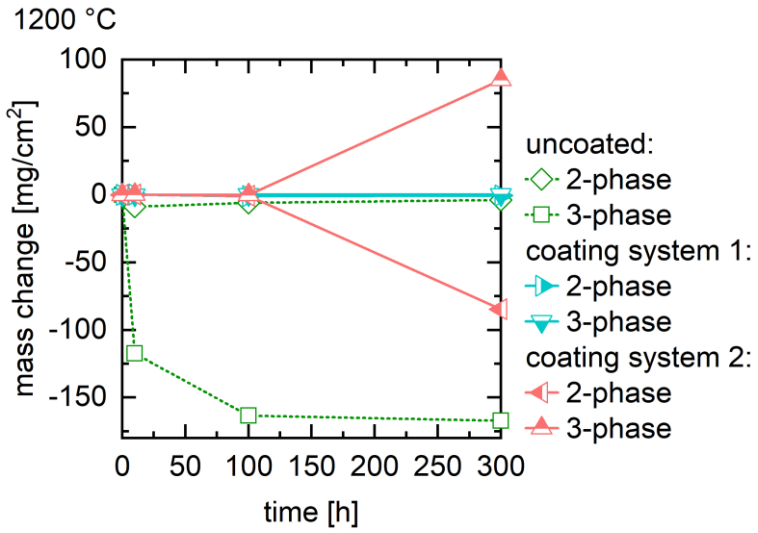

Figure 4

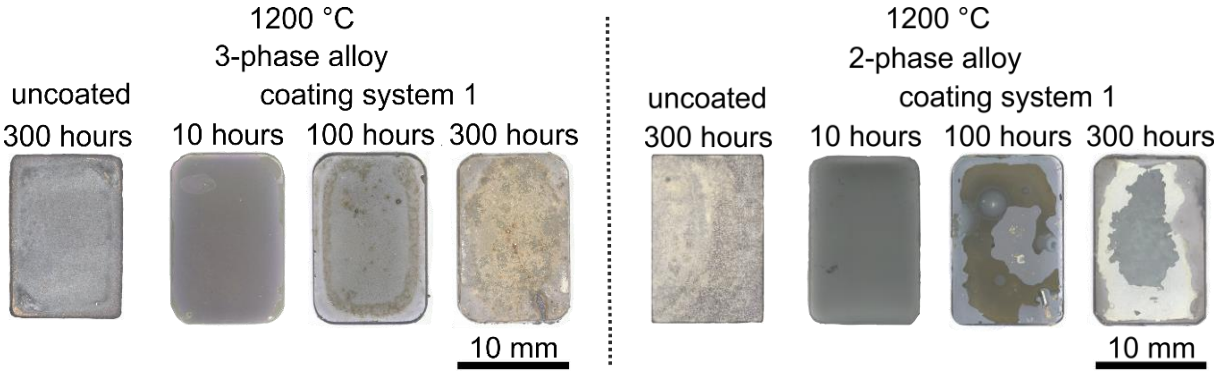

Figure 5

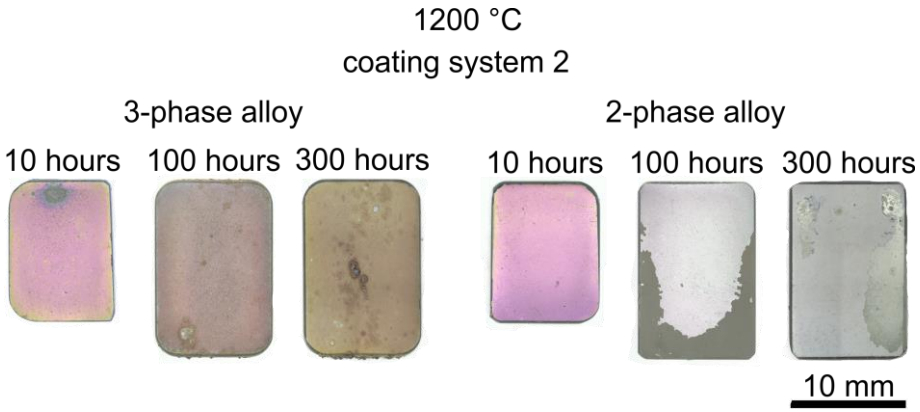

Figure 6

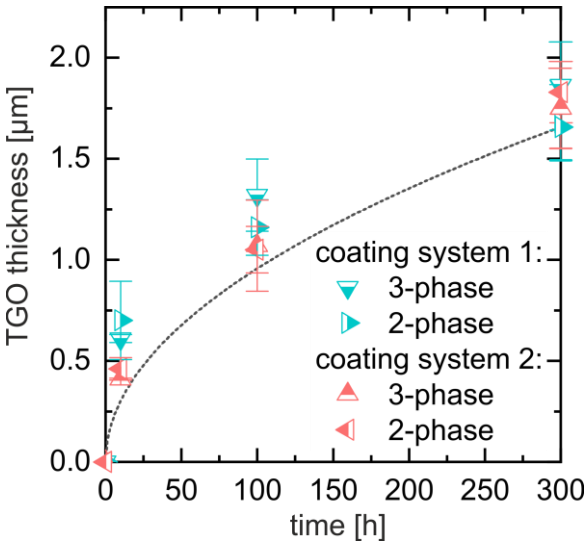

Figure 7

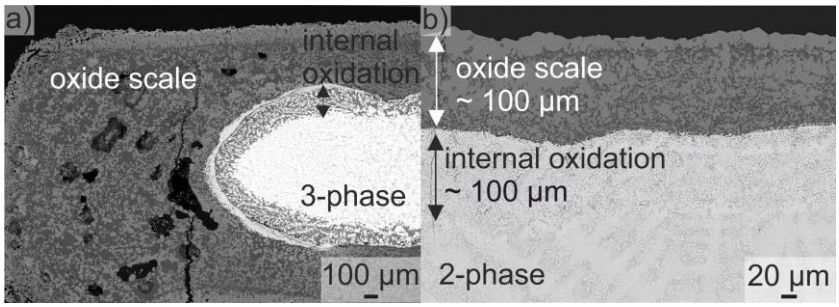

Figure 8

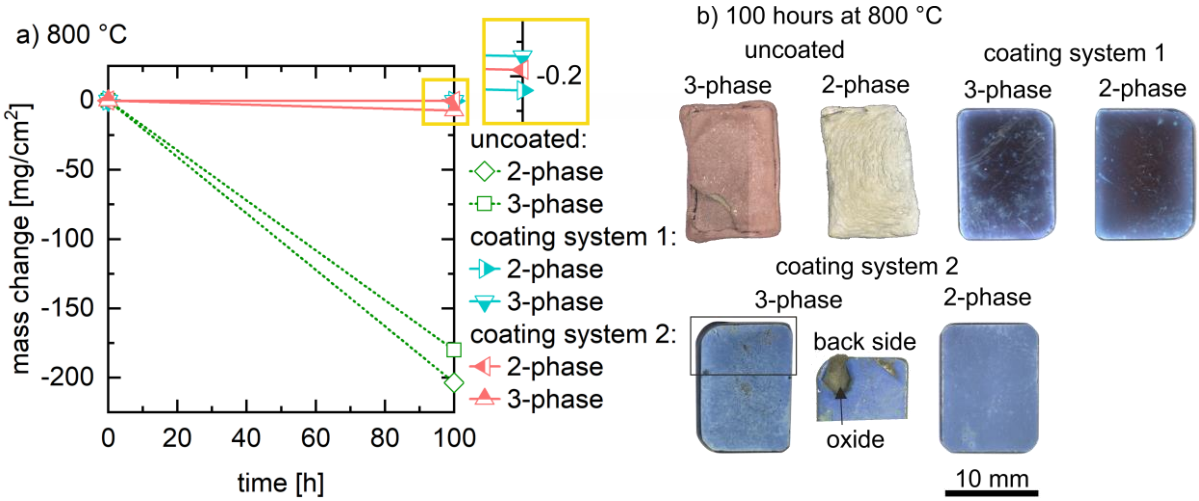

Figure 9

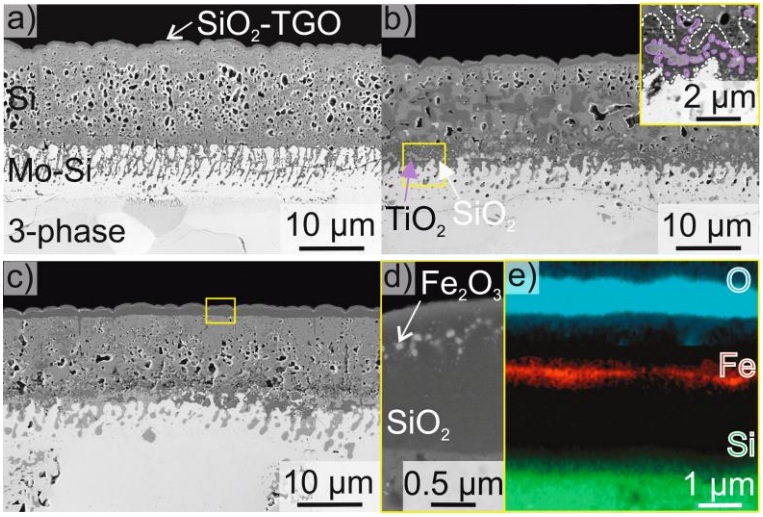

Figure 10

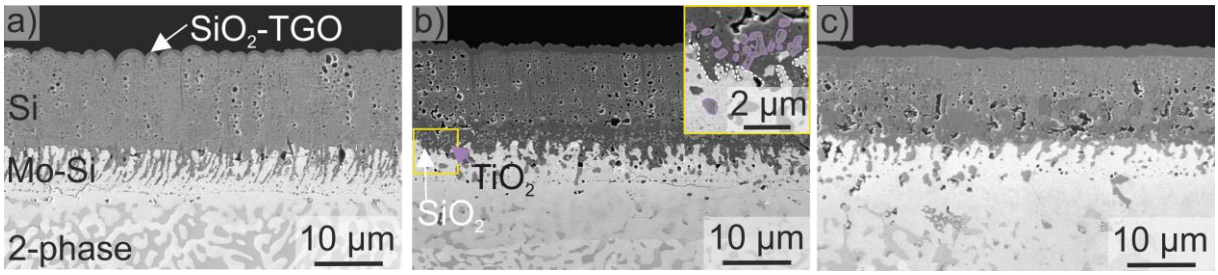

Figure 11

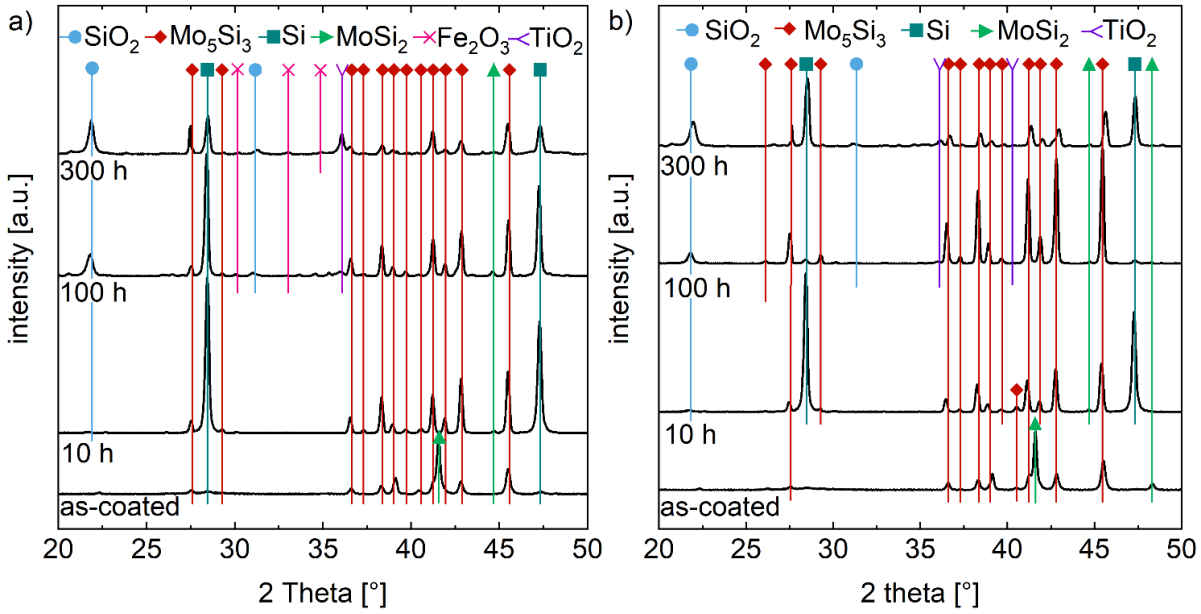

Figure 12

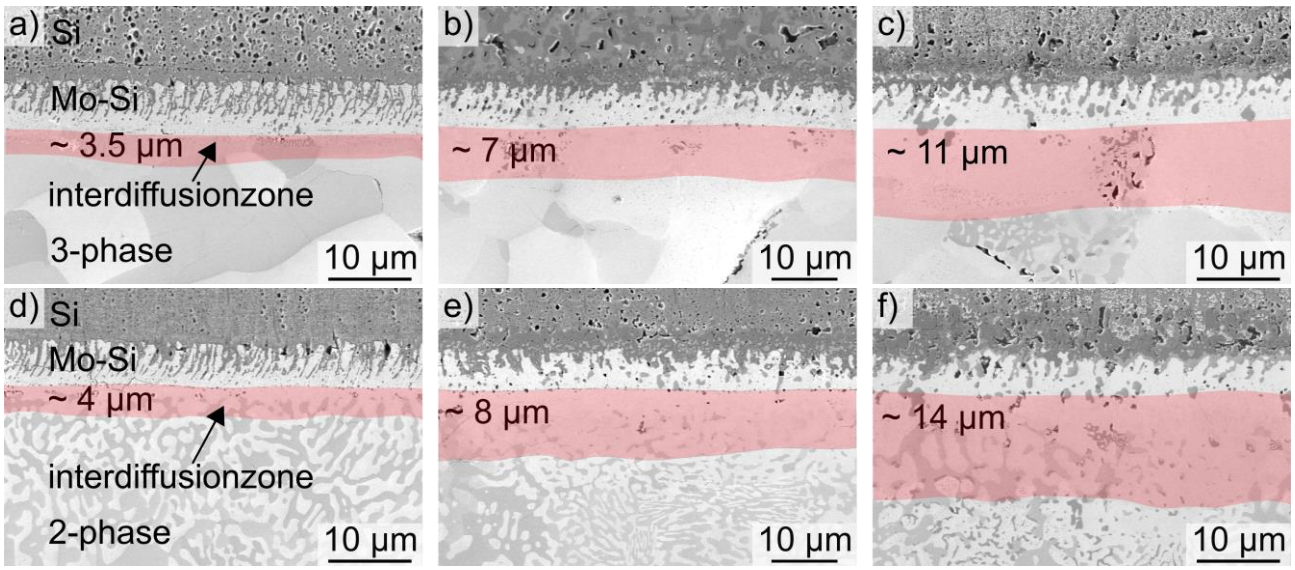

Figure 13

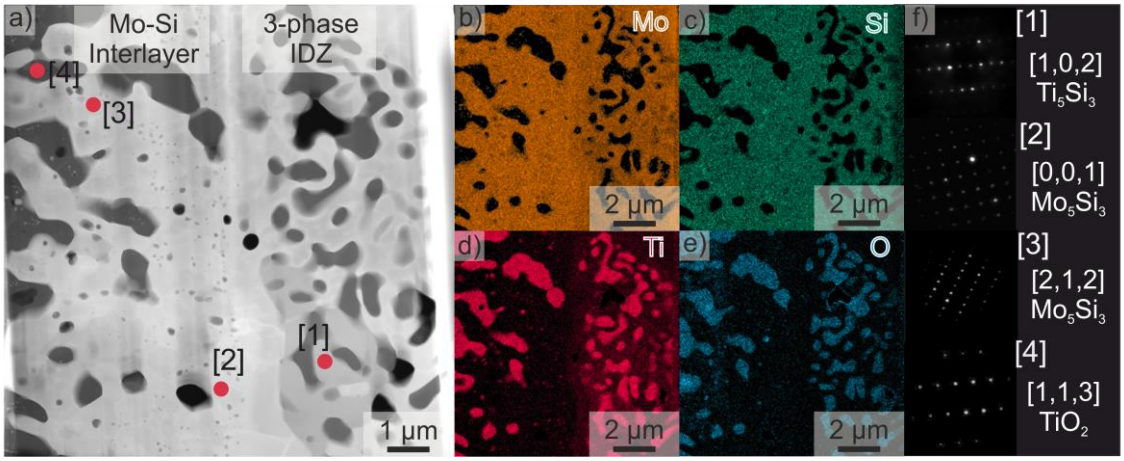

Figure 14

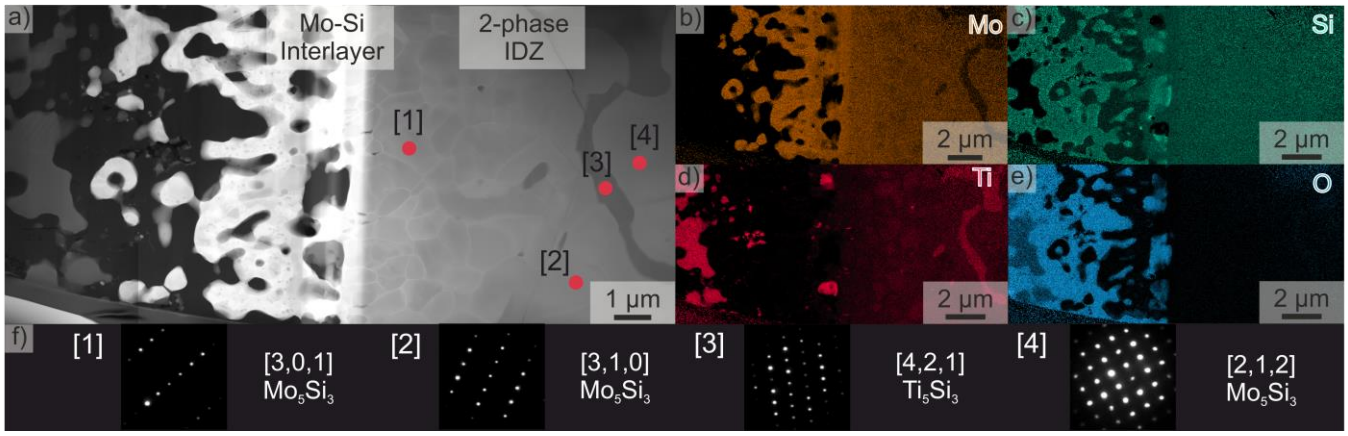

Figure 15

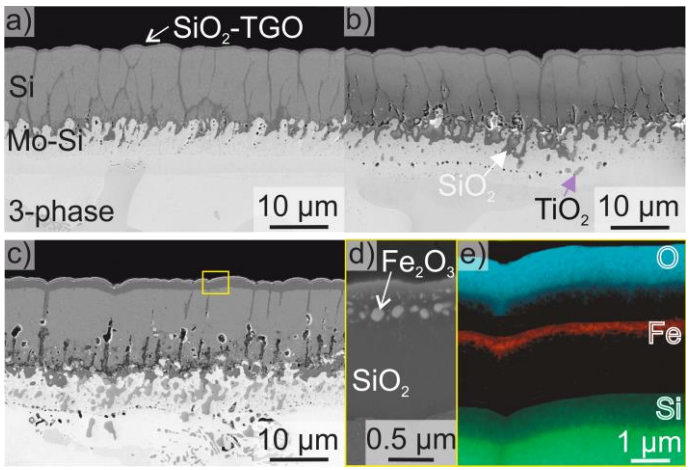

Figure 16

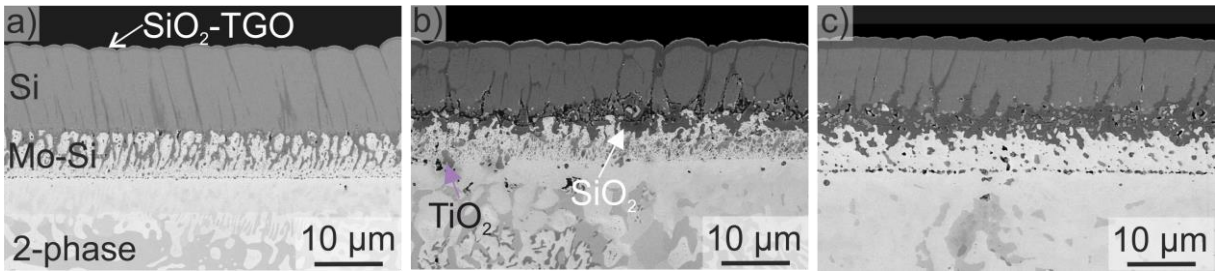

Figure 17